CloudViT: classifying cloud types in global satellite data and in kilometre-resolution simulations using vision transformers.

Julien LENHARDT [1], Johannes QUAAS [1,2], Dino SEJDINOVIC [3], Daniel KLOCKE [4]

[1] Leipzig Institute for Meteorology, Universität Leipzig, Leipzig, Germany

[2] ScaDS.AI - Center for Scalable Data Analytics and Artificial Intelligence, Leipzig University, Humboldtstraße 25, 04105 Leipzig, Germany

[3] School of Computer and Mathematical Sciences & Australian Institute for Machine Learning, University of Adelaide, Adelaide, Australia

[4] Max Planck Institute for Meteorology (MPI-M), Hamburg, Germany

Correspondence to: Julien LENHARDT (julien.lenhardt@uni-leipzig.de)

Abstract

Clouds constitute, through their interactions with incoming solar radiation and outgoing terrestrial radiation, a fundamental element of the Earth's climate system. Different cloud types show a wide variety in cloud microphysical or optical properties, phase, vertical extent or temperature among others, and thus disparate radiative effects. Both in observational and model datasets, classifying cloud types is also of large importance since different cloud types respond differently to current and future anthropogenic climate change. Cloud types have traditionally been defined using a simplified partition of the space determined by spatially aggregated values e.g. of the cloud top pressure and the cloud optical thickness. In this study, we present a method called CloudViT (Cloud Vision Transformer) building upon spatial extracts of cloud properties from the MODIS instrument to derive cloud types, leveraging spatial features and patterns with a vision transformer model. The classification model is based on global surface observations of cloud types. The method is then evaluated through the distributions of cloud type properties and the corresponding spatial patterns of cloud type occurrences for a global cloud type dataset produced over a year-long period. Subsequently, a first application of the cloud type classification method to climate model data is presented. This application additionally provides insights into how global storm-resolving models are representing clouds as these models are increasingly being used to perform simulations. The global cloud type dataset and the method code constituting CloudViT are available from Zenodo (Lenhardt et al., 2024b).

1 Introduction

Clouds form an essential component in the Earth's climate, by impacting the atmospheric energy budget and water cycle, and by influencing the reflected solar radiation as well as the outgoing terrestrial radiation fluxes. Clouds are highly variable spatially and temporally, and occur in a large variety of types (Howard, 1803; WMO, 2017). Stratiform and cumuliform clouds, in low, medium or high levels, have all very different effects on radiation and precipitation formation. This is one of the causes for the uncertainties in estimates of their response to anthropogenic climate change both currently and in the future (Boucher et al., 2013; Forster et al., 2021). These uncertainties manifest both in observational datasets for which the aim is to constrain past and current effects, and in climate models where cloud representation is of utmost importance to properly constrain future scenarios. Through the phase (liquid, ice or mixed), the droplet size distribution, the vertical structure or other micro- and macro-physical properties, different cloud types can lead to drastically diverse radiative effects making the cloud type a property of interest to help describe their involvement in the weather and climate system. Unravelling and understanding trends in clouds has become more tractable in recent decades due to the large amount of remote sensing data made available globally on a daily basis. However, analysing such extensive datasets manually becomes challenging, especially with the goal of extracting meaningful information about different cloud types based on their patterns, microphysical properties or radiative effects. Algorithms have taken over this complex task but still struggle to provide objective groupings out of the intricate spatio-temporal patterns observed in remote sensing data. At the same time, applying methods to climate models which are engineered on remote sensing data could become more viable as new global climate models are bridging the gap by reaching km-scale resolutions.

Traditional cloud classification methods are built on simple characteristics. The standard classification developed as part of the International Satellite Cloud Climatology Project (ISCCP) relies on three levels (low, medium, high) of cloud altitude using as proxy the cloud top pressure (CTP) and three thresholds of cloud optical thickness (COT), defining overall nine cloud types (Rossow et al., 1991). This classification is performed pixel-wise, setting aside any spatial pattern in the cloud field from which information could be obtained to better inform the classification process. Relying on the same type of two-dimensional histograms, recent methods have been developed aiming at refining the created clusters and partially relaxing the constraints on the pre-defined thresholds (Tzallas et al., 2022). The reason to choose the two parameters is that such a classification lends itself to the analysis of cloud radiative effects: the cloud radiative effect in the solar is a monotonic function of COT, the one in the terrestrial spectrum, of CTP. However, one might be interested in sensitivities of cloud thickness or water content to different drivers (e.g., aerosols) for given cloud types, which is hampered by using CTP and COT to define the types. Also, COT does not map well onto the distinction between cumuliform and stratiform clouds. For such reasons, Unglaub et al. (2020) defined cloud regimes from cloud base height and variability in cloud top height, hinting at the added value of some measure of spatial variability and pattern. However, to leverage spatial structure and textures, cloud classification methods based on artificial intelligence (AI) have opened new avenues of research built upon vast amounts of remote sensing data. For example, using convolutional neural networks (CNNs; LeCun et al., 1989; LeCun et al., 1995), Zhang et al. (2018) used ground-based imagers and human-labelled cloud types, Rasp et al. (2020) classified clouds from expert-labelled satellite images of four different cloud organisation patterns in the trades and Kuma et al. (2023) built on shortwave and longwave radiation satellite retrievals and ground-based observations. Relying on similar model architectures, Zantedeschi et al. (2019) and Kaps et al. (2023) classified cloud types derived from active remote sensing labels. Other methods have, on the other hand, been developed without the use of labels, drawing conclusions from clusters appearing in large remote sensing radiation retrievals (Kurihana et al., 2022). While computer vision models have proven to perform satisfactorily with respect to their respective labelled (or not) datasets, developing a method further drawing upon large datasets of ground-based observations and satellite retrievals and additionally being transferable to climate model simulations could prove to be an asset in evaluating cloud types and their representation in both observational and climate models datasets.

In this study, we investigate the classification of clouds by merging surface observations of cloud types and passive satellite retrievals of cloud properties, building a method called CloudViT (Cloud Vision Transformer). Following a similar methodology from previous work (Lenhardt et al., 2024a), we define cloud scenes as tiles of 128x128 km² which encompass cloud microphysical and optical properties at a 1 km horizontal resolution. The employed cloud properties are from the MODerate Resolution Imaging Spectroradiometer (MODIS, Platnick et al. (2017)), and more particularly the cloud top height (CTH), the cloud optical thickness (COT) and the cloud water path (CWP), which are paired with surface network observations of cloud types (cf. Table 1). To harness the spatial aspect of the cloud scene and extract relevant features from the input cloud properties, we resort to computer vision models based on CNNs and transformers (Dosovitskiy et al., 2020). Firstly, a vision transformer model is trained in a self-supervised setting to create a condensed latent representation of the input cloud field. Subsequently, a simpler classification model is fitted to predict the cloud type corresponding to the cloud scene, learning from the labels of a

82 wide ground-based observation network. The formulated method has the goal to produce robust retrievals of cloud types while
83 generalising from the local ground observations to global distributions, increasing both the temporal and spatial coverage. The
84 method relies partly on the assumption that the observed cloud types exist on scales similar to the extent of the tiles, and
85 additionally builds on the spatial patterns characteristic of different cloud types. Moreover, as the ground-based cloud type
86 observations provide consistent labels which are only available at sparse locations, we can leverage long-standing instruments
87 like MODIS to design an algorithm based on satellite retrievals suited to generalisation to global distributions.

88 Firstly, we introduce in section 2 the different datasets used in the study alongside the colocation process between the
89 ground-based and satellite datasets. Subsequently, the different components of the CloudViT method are presented in section 3,
90 supported by sensitivity studies about the generalisation skill of the models and the benefits of the spatial context. In section 4,
91 we evaluate the method and investigate the distribution of cloud properties following the predicted cloud types. The results in
92 section 5 focus on the extension to a global distribution of cloud types and present a first application to climate model data.
93 Eventually, we discuss the benefits of the presented method, the potential improvements and the remaining challenges.

2 Data

2.1 Surface observations

98 The cloud type observations used in this study come from two similar global observation datasets maintained by the UK Met
99 Office, one providing observations made at sea (Met Office, 2006) and the second providing observations made on land (Met
100 Office, 2008). These observations are performed from weather stations (land or sea) or ships, by trained observers following the
101 WMO code tables (WMO, 2019). Each cloud level (high, WMO code table 0509; medium, WMO code table 0515; low, WMO
102 code table 0513; see Table A.1) is separated in 9 different types describing in more detail the aspect and type of the observed
103 clouds. The labels thus provide a high level of precision regarding the observed cloud scene from the surface. Naturally, the case
104 of multilayer clouds poses a problem since the field of view and the visibility from the surface are limited, which is why we
105 remove the potential multilayered cases from the training dataset to focus only on single-layer observed cloud scenes. It induces
106 potential selection bias issues as some cloud types might more likely be observed in multilayered configurations. The relative
107 amounts of each cloud type before and after the filtering and colocation process are displayed in Figure 2. Similarly, uncertainty
108 is greater for medium and high clouds as their observation can be more challenging than for low clouds. Furthermore, the spatial
109 distribution of the labels (Fig. 1, Fig. A.1) can be problematic as the marine observations are distributed mainly along ship
110 routes. On the other hand, combining that with land observations provides a more complete representation of cloud types,
111 especially for high level ones, all the while introducing the influence of orography. Other studies like Kuma et al. (2023) and
112 Lenhardt et al. (2024a) have built skilled retrievals of cloud quantities based on these ground-based observation datasets,
113 overcoming limitations pertaining to incomplete field of view and disparate spatial distribution.

114 For simplifying the analysis but also the training of the classification model, we group the 27 reported WMO cloud types into 4
115 and 10 categories, similarly to Kuma et al. (2023). The first categorisation allows for broad classification by dividing the cloud
116 species into high, medium, cumuliform and stratiform types. The second categorisation provides a more detailed classification
117 while still limiting the subdivision of similar cloud types. This prevents a too pronounced unbalance in the cloud type labels
118 while possibly removing some of the subjective biases and uncertainty stemming from the human observers. The detailed
119 categories corresponding to the WMO codes are available in Table A.1 and shown in Figure 2.

2.2 Satellite retrievals

123 In addition to the surface observations, we use satellite retrievals from MODIS, in particular from the AQUA satellite. MODIS
124 retrievals offer a vast amount of data at kilometre-scale resolution with daily overpasses. Each of the supplied granule file
125 contains cloud microphysical and optical properties across a region with a span of around 2330 km x 2000 km. We make use of
126 the available CUMULO dataset (Zantedeschi et al., 2019) since it allows access to preprocessed MODIS level 2 satellite data,
127 with global coverage, and for two full years (2008 and 2016). Among the data variables available, we rely on two unified
128 products (cf. Table 1) describing either cloud properties (MODIS06 level 2 cloud product, hereafter MYD06; Platnick et al.,
129 2017) or the cloud cover (MODIS35 level 2 cloud flag mask, hereafter MYD35; Ackerman et al., 2017). The latter's main usage
130 is to help screen for cloud scenes with a minimum cloud coverage.

131 The MYD06 data product incorporates miscellaneous properties pertaining to the cloud top (temperature, pressure, height)
132 alongside some microphysical and optical properties (effective radius, water path, optical depth). As mentioned previously, our

133 method builds upon level 2 data which are typically obtained from calibrated radiances through methods described in Platnick et
134 al. (2017). More specifically, cloud top properties are retrieved using several radiance channels: harnessing the opacity of CO_2,
135 the CTP of high clouds is retrieved with wavelengths in the CO_2 absorption range, while infrared wavelengths combined with
136 simulated brightness temperatures are used for lower and thicker clouds. The related CTH retrieval can thus suffer from regional
137 biases as the brightness temperatures are based on vertical profiles from reanalysis using regional and monthly averaged lapse
138 rate data along with surface temperature (Baum et al., 2012). The method introduced here can thus incorporate said biases from
139 the input data into the learning process. The microphysical and optical properties of clouds - COT and cloud effective radius
140 (CER) - are retrieved concurrently from multispectral reflectances, CTP values, surface types and cloud masks. Lastly, the CWP
141 is also retrieved as part of the cloud optical properties algorithm detailed in Platnick et al. (2017). The additional input quantities
142 needed to derive and retrieved the mentioned cloud properties (e.g. water vapour and ozone vertical profiles from reanalysis;
143 Platnick et al., 2003; Baum et al., 2012) can result in subsequent uncertainties where only sparse observations like in remote
144 marine areas are available for the data assimilation. Eventually, from the entirety of available MYD06 retrievals, we select three
145 cloud properties in particular, namely the CTH, COT, and CWP.

146 As a whole, the MYD06 product has the advantage that, building directly on cloud properties, we can design a classification
147 model from which the relationship between cloud type and other cloud properties can then be examined. Relying on calibrated
148 radiances which lie ahead in the retrieval process could offer a more neutral input but due to the large associated dimensionality,
149 extracting information about clouds might become more challenging. Additionally, basing the method on commonly used cloud
150 properties allows us to directly associate the results with other derived cloud classifications, making the comparison and
151 understanding of the predictions more straightforward. Nevertheless, the biases introduced by using level 2 data in comparison to
152 level 1 calibrated radiances and reflectances should be properly characterised and taken into account in the behaviour of the
153 statistical model.

154 Alongside the colocated dataset, we build a collection of randomly sampled tiles out of the satellite retrievals from the year 2008.
155 For each granule, a maximum of 20 tiles are sampled while ensuring the amount of missing data stays limited. This process leads
156 to the compilation of more than 1.3M single tiles of cloud properties. These tiles are then randomly split temporally into training
157 (70%), validation (10%) and test (20%) sets. This dataset is the basis for the self-supervised training procedure presented in the
158 following section.

159

Data product	Description	Variables	Resolution	Usage
Global marine meteorological observations (Met Office, 2006)	Marine surface observations	Cloud type	Latitude/longitude coordinates 0.1° Hourly/daily observations	Labels
Land SYNOP reports (Met Office, 2008)	Land surface observations	Cloud type	Latitude/longitude coordinates 0.1° Hourly/daily observations	Labels
MODIS Atmosphere L2 Cloud Product (MYD06) (Platnick, 2017)	Cloud-top properties, cloud optical and microphysical properties	Cloud top height, CTH (m) Cloud optical thickness, COT (a.u.) Cloud water path, CWP ($g.m^{-2}$)	1-km pixel resolution Daily overpass	Input features
MODIS Atmosphere L2 Cloud Mask Product (MYD35) (Ackerman, 2017)	Cloud pixel flag	Cloud mask	1-km resolution Daily overpass	Used for cloud scene filtering

160 **Table 1 : Datasets description. The surface observations are provided by a worldwide station network available from the**
161 **UK MetOffice (Met Office, 2006; Met Office, 2008; see section 2.1). The MODIS data are derived from the collection 6.1**
162 **of the datasets (Ackerman, 2017; Platnick et al., 2017; see section 2.2).**

163

Marine (2008, 2016) & land (2016) cloud type observations count
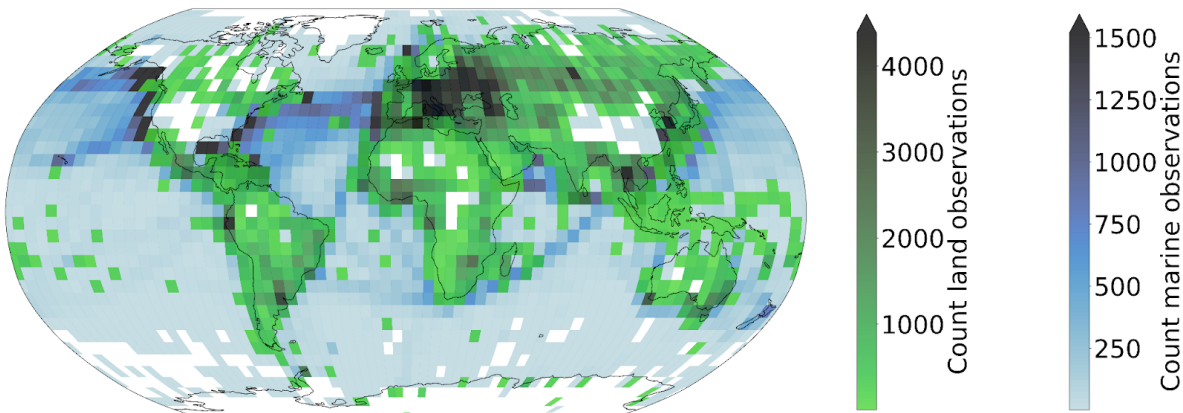
Figure 1: Spatial distribution of cloud type observations for marine (years 2008 and 2016; Met Office, 2006) and land (year 2016; Met Office, 2008).
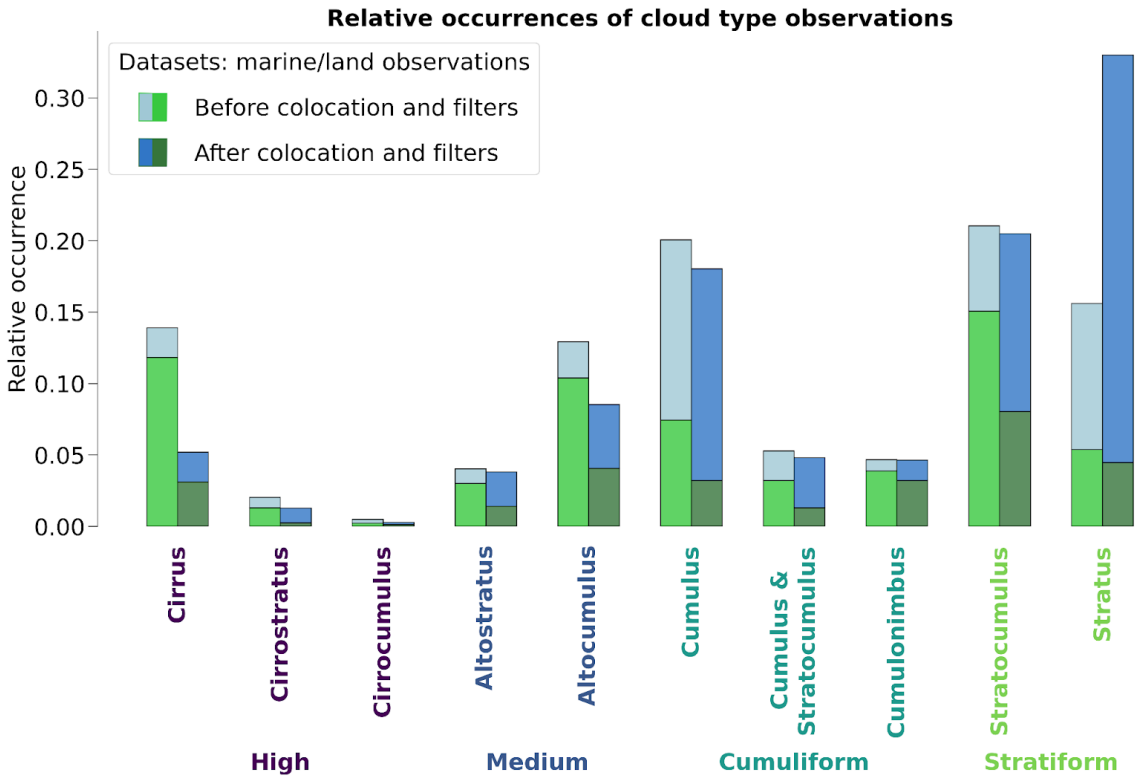
Figure 2: Relative occurrences of cloud types before and after the colocation and filtering process, indicated for both the marine (blue; Met Office, 2006) and land (green; Met Office, 2008) observational datasets. The x axis corresponds to the cloud types in the case of 4 and 10 categories.

3 Method

3.1 Method outline

Building on computer vision models and their substantial amount of trainable parameters usually requires adapting the training strategy when the available dataset is of modest size. In the presented study, the amount of labels available is greatly reduced during the colocation process but still contains useful and exploitable information about the observed cloud types. We thus introduce a self-supervised learning process which allows us to draw on the larger amount of satellite data available before addressing the more complex task of cloud classification. The larger purpose of this methodology is to be able to classify clouds on a global scale, outside of the areas where surface observations were made and outside of the typical coverage of human observation stations.

For the self-supervised task, we train two models to reconstruct 3D data cubes of cloud properties. The first model, which is used as a baseline, is a CNN backbone we previously presented in Lenhardt et al. (2024a) to handle satellite retrievals of cloud properties for cloud base height prediction. The second model we develop in this study is based on vision transformers (Dosovitskiy et al., 2020), a recent type of model compared to the more typical CNNs for computer vision applications. The spatial pattern of the cloud properties and their scale provide information about clouds, which can be leveraged to classify them for example into more stratiform and more cumuliform types. During the training phase of these models, the samples are images of size 128x128 km² and 128x128 pixels consisting of three different cloud properties: CTH, COT and CWP. We ensure that the models learn to distinguish cloud patterns and not to recognise specific geographical locations by extracting samples randomly across global satellite retrievals from the year 2008, without adding information about their location. In a second step, a classification model is trained on the colocated samples of cloud properties and surface observations. As mentioned in section 2.1, the number of types reported in the observations for clouds is reduced to either 4 or 10 classes (Kuma et al. 2023). The training process follows a supervised learning framework, where the classification model outputs a single cloud type (among the 4 or 10 cloud types) for the whole extent of the input cloud scene of size 128x128 km² and 128x128 pixels. The benefit of the presented method using either a CNN or a vision transformer, which are models with some degree of spatial awareness, is that it is consistent with the cloud type identified by the human observer. Furthermore, in comparison to conventional methods like the ISCCP, the method benefits from a potential ability to distinguish more detailed cloud types without using predefined thresholds.

3.2 Vision transformer

Vision transformers were introduced by Dosovitskiy et al. (2020), building on the transformer architecture previously presented in Vaswani et al. (2017) which was mainly applied to natural language processing (NLP) tasks. The adaptation to images was made by splitting images into patches of a certain size, 16 pixels in the case of the seminal paper, and providing the sequence of embeddings of these patches to a transformer. The patches from the images are then treated as words would be in a NLP application. The transformer can then be trained in a supervised fashion to classify the input images. They have been shown to perform at the same level or even outperform classical computer vision models like ResNets on tasks like classification (e.g. see Section 4 of Dosovitskiy et al., 2020). However, as mentioned in section 3.1, this type of model, alongside CNNs, are data hungry and require a large amount of labelled samples to be trained from scratch in a supervised fashion. In this setting, self-supervised pretraining can lead to highly performant models while not requiring a larger training dataset. We train a vision transformer following the self-supervised pretraining methodology presented in Atito et al. (2023), named Self-supervised vision Transformer (SiT). This methodology allows to train vision transformers in a self-supervised fashion building on the concept of Group Masked Model Learning (GMML), additionally using the same autoencoder framework as with traditional CNNs like the commonly used U-Net (Ronneberger et al., 2015) or our baseline model from Lenhardt et al. (2024a). We do not adapt the presented architecture of the SiT which was adopted directly from the initial vision transformer architecture, apart from the latent dimension which is set to 256 similarly to the CNN built in Lenhardt et al. (2024a).

One strength of the transformer architecture is the possibility to easily include several simultaneous learning tasks. We can use this ability to our advantage and incorporate two objectives for the self-supervised training process: input reconstruction following GMML and contrastive learning. The input reconstruction is achieved by adapting the transformer into an autoencoder architecture. Like with traditional CNN autoencoders, the task is for the model to reconstruct the provided input. We benefit further from another advantage of vision transformers as they showcase a reduced complexity compared to CNNs since they rely to a much lesser degree on convolution operations. The methodology of Atito et al. (2023) additionally uses recent results in GMML to further help in the self-supervised learning task. The framework of GMML is integrated in the reconstruction task by

225 replacing random parts of the input image with noise. The overarching goal of this image modification is to train the model to
226 learn semantic representations of the input data, allowing reconstruction of masked areas only with knowledge of some other
227 patches in the input image. The objective for this reconstruction task hence takes the form of the l1-loss, a commonly used metric
228 (Zhao et al., 2016) between the standardised input and the reconstructed output:

229
$$L_r \;=\; \frac{1}{N} \sum_{i=1}^{N} \left\| x_i \;-\; D_\theta(E_\theta(x_i^c)) \right\| \qquad (1)$$

230 where x_i is the input standardised image, x_i^c is the corrupted standardised image, $||.||$ is the l1-loss, N is the batch size, D_θ and E_θ
231 are namely the decoder and encoder parts of the model with θ designating their learnable parameters.

232 The second learning task included in the training process is based on contrastive learning. Since the presented self-supervised
233 process does not rely on labels for the training data contrary to the vision transformer from Dosovitskiy et al. (2020), the learning
234 task needs to be adapted. To this extent, several geometric transformations and perturbations are applied to the training samples
235 for which the transformer should produce similar outputs. The synthetic pairs can then be used as matching pairs and a metric
236 can be built measuring their similarity. The contrastive task is thus training the model to minimise the distance between matching
237 pairs of sample and corresponding augmented sample, while maximising the distance between different samples in the batch.
238 Atito et al. (2023) propose to use as a contrastive metric the arithmetic mean over the matching pairs in the batch of the cross
239 entropy of their normalised similarities:

240
$$L_c \;=\; -\frac{1}{N} \sum_{i=1}^{N} \log l_c(x_i, \, x_i^a, \, E_\theta, \, D_\theta) \qquad (2)$$

241 where the similarity metric between a sample x_i and its augmented version x_i^a is the normalised temperature-scaled softmax
242 similarity (Chen et al., 2020). The actual process of the contrastive learning further requires the use of a momentum encoder to
243 generate different views of the samples and their augmented pendants.

244 The integral self-supervised training process consists in a combination of the two previously presented learning tasks. For each
245 batch of samples, we create augmented versions of the samples which together constitute matching pairs. GMML corruptions are
246 applied to both samples and the model is subsequently trained to reconstruct the original inputs from these corrupted samples. At
247 the same time, the similarity between matching pairs of samples is maximised. The complete loss function thus takes the form of:

248
$$L = \alpha \times L_r + L_c \qquad (3)$$

249 where α is a scaling factor between the two tasks. We follow the recommendation of Atito et al. (2023) to set $\alpha = 5$ in the case
250 of small-scale datasets so that the vision transformer can learn enough of the local inductive bias.

251 We set out to examine in further detail the ability of the vision transformer and of the self-supervised training methodology by
252 evaluating how different configurations of the input data and of the model architecture can impact the quality of the learnt
253 representations and the transfer to cloud classification. We mainly discuss in this section the reconstruction skill of the vision
254 transformer and the potential influence of contrastive learning. The transfer to the cloud classification task will be described in
255 the following section where fine-tuning to the downstream task or the use of external models are surveyed. Since training vision
256 transformers requires large computing resources, we limit ourselves for all the pretraining processes to only 10% of the initial
257 dataset mentioned in section 2.2, similar to what is done in Atito et al. (2023) regarding ablation studies.

258 To begin with, we investigate how the two architectures of vision transformers fare during the self-supervised training and how
259 the scaling factor between the contrastive loss and the reconstruction loss impacts the learning process. The two architectures
260 tested correspond to the small variant of the vision transformer from Atito et al. (2023) and the base variant from Dosovitskiy et
261 al. (2020). To offer an overview on each model's complexity, their respective numbers of parameters are 21M and 86M, the main
262 difference originating from the number of heads in the self-attention layers, the size of the multi-layer perceptron (MLP) and the
263 hidden dimension. We additionally investigate the self-supervised training process by using pre-trained weights made available
264 in Atito et al. (2023) for which the pretraining was done on a computer vision task, the ImageNet-1K dataset (Deng et al., 2009).
265 However, the pretrained weights of the ImageNet-1K dataset are only made available for the small variant of the vision
266 transformer. An additional comparison is done with a model trained only on the colocated dataset using the small variant. The
267 contrastive and reconstruction losses for the different model setups are detailed in Figure B.1. Firstly, we notice that the model
268 trained solely on the colocated dataset would need more epochs to reach similar performance compared to all the other setups. As
269 the colocated dataset contains two orders of magnitude less samples than the training dataset, the model has also seen much less
270 data after 10 epochs, hindering the training process most notably for the contrastive loss. Even after further training the model on
271 the colocated dataset for 150 epochs, it is struggling to match the other models trained on the complete training dataset with best
272 contrastive and reconstruction losses of 0.95 and 0.23, respectively. On the other hand, the other setups reach similar

performance in both contrastive and reconstruction losses after 10 epochs. The model with pretrained weights displays better performance right from the start of the training process but improves only marginally thereafter. This could be explained by the fact that using the pretrained weights allows the model to capture already well the structure and patterns of the clouds in the remote sensing data even though their modality is different from the one seen in the ImageNet-1K dataset. It thus shows the strength of transfer learning in computer vision tasks. Nevertheless, we can observe that for the pretrained model both the contrastive and reconstruction losses are reaching a plateau after only a few epochs while the other model setups display a negative gradient indicating further learning capabilities. Focusing on the different variants trained with scaling factors of 1 or 5, we notice that the choice of a larger scaling factor leads to better reconstruction skill while losing almost no performance with respect to the contrastive loss.

Eventually, we decide to use as model the small variant of the vision transformer with a scaling factor α of 5, as it showcases good performance in both tasks during the training while having a number of parameters four times smaller than the base variant. Furthermore, the self-supervised training task on the large unlabelled dataset allows the model to have plenty of data to learn from, the pre-trained model weights giving only marginal gain for a few epochs at the start. The small variant of the vision transformer was shown to perform very well on a large variety of tasks as per the results from Atito et al. (2023). The results across the training, validation and test datasets are shown in Figure 3 for the training process and some examples of reconstructed samples belonging to all three splits, while Figure 4 highlights the spatial distribution of the reconstruction error per channel and across splits.
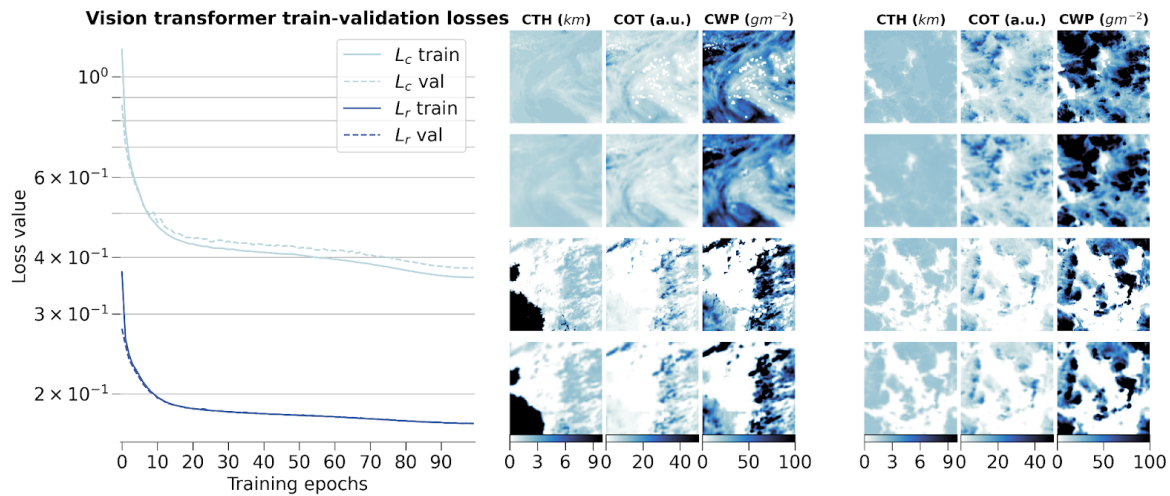
Figure 3: (left) Training and validation losses during model optimization for the small variant of the vision transformer on the global training dataset. (right) Examples of tiles (first and third rows) with the corresponding reconstructions (second and fourth rows) for the different cloud property channels.

Ultimately, we can compare the skill of the vision transformer to that of the baseline CNN autoencoder from Lenhardt et al. (2024a). The CNN autoencoder was trained using as reconstruction error the mean squared error (MSE) on similar MODIS data but only with MODIS granules over the ocean. It was shown to perform similarly with a slightly higher error over land when evaluated over a global dataset. The vision transformer model outperforms the CNN autoencoder on all metrics (MSE and l1-loss) across all data splits (training, validation and test), displaying consistently across data splits on average an MSE of 0.15 and a l1-loss of 0.12 compared to 0.3 for both metrics for the CNN. Examples of reconstructed samples additionally show how the l1-loss helps produce sharper edges in the reconstruction, a well-known issue with the application of MSE as target metric in computer vision (Zhao et al., 2016). The contribution to the error comes mostly from the COT channel for both models and the error is concentrated in areas of higher variability for the respective channels. The metrics values are summarised in Table B.1. The spatial generalisation skill, alongside the sensitivity to the tile size and the impact of data augmentation on the performance on the cloud classification task are analysed in the following section.
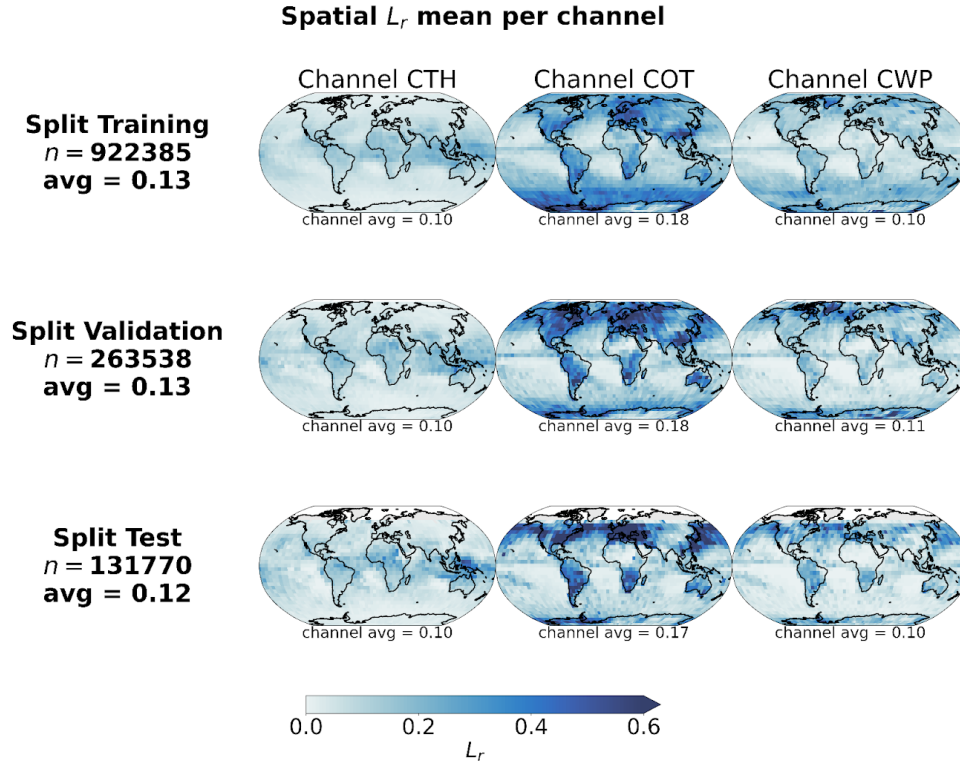
**Figure 4: Spatial distributions of mean channel reconstruction errors for CTH, COT and CWP, aggregated on a 5°
regular grid for the training, validation and test datasets.**

3.3 Cloud type classification

The next task at hand is the cloud type classification, building on the colocated samples of satellite retrievals and surface
observations. For the two years of MODIS AQUA data available, out of 104 823 colocated samples we retain only 11 094 for our
training and testing datasets after filtering, among others, for missing data - typically 50% of the samples are discarded, mainly
when the colocated observation lies on the edges of the satellite granule - and single layer cloud observations as reported by the
observer - around 60% of the previously filtered samples are kept. The cloud type observations are then regrouped into 4 or 10
types as mentioned previously. The rest of the study will focus on these categories as targets. From the latent space
representations produced by the vision transformer or the CNN autoencoder, we build a classification model either by attaching a
classification head to the encoder network or by using a simpler classification model like a random forest (RF; Breiman, 2001).
To investigate the performance of the classification models on the two classification tasks at hand (4 and 10 cloud types), we use
different metrics tailored to unbalanced classification setups as the cloud types are not equally represented (see Table A.1). A
first method to assign similar weight to all classes regardless of the class' cardinal is to use macro-averaged metrics. In this
framework, the metric of interest is averaged over the samples of each class separately before being averaged over the classes.
This leads to a higher weight for minority classes for which the model might perform differently, usually worse, compared to the
majority classes providing different information over traditional averaging strategies (micro-averaged for example) where the
result will be dominated by the samples from the majority classes. We report several metrics adapted to an unbalanced setting:
the index balanced accuracy (IBA; Garcia et al., 2012) of the geometric mean, the macro-averaged accuracy and the
macro-averaged f1-score.
For the classification model we investigate two alternatives: a RF classification model (implementation from *Scikit-learn*
package, Pedregosa et al., 2011) and a MLP classification head (Hinton, 1989; implemented in *PyTorch*, Paszke et al., 2019).
However, a wider diversity of classification models could be implemented based on the backbone provided by the vision
transformer. The RF model provides simplicity in the implementation and the training process, while the MLP is the typical
architecture used for the downstream task following a network like a vision transformer or a CNN. The RF model has 10 or 25

335 trees, for the cases of 4 and 10 cloud types respectively, with a maximum depth of 5. Basic hyper-parameter optimization showed
336 that with the reduced amount of samples and the limited variety in cloud scenes for some categories (even more with balanced
337 classes, see section 3.3.3), models displaying limited complexity avoided overfitting and generalised better on unseen data. The
338 MLP consists of two fully-connected layers (hidden dimension 4096) with a Gaussian Error Linear Unit (Hendrycks & Gimpel,
339 2016) in between and is trained using the cross-entropy loss. The sensitivity studies and experiments are done only using RF
340 models but the evaluation in the subsequent section will be done on both types of classification methods. Various sensitivities
341 could be explored in the presented setting but we here focus on the potential benefit of the spatial context, the ability to
342 generalise spatially to unseen locations and the impact of balancing the labelled dataset.

3.3.1 Spatial context and tile size

345 We look at the influence of the input size by training vision transformers (small variant) on different sizes of inputs namely
346 128x128, 64x64, 32x32 and 16x16. We do not consider larger tile sizes as the cloud scene might then be less representative of the
347 surface observation, especially since we only consider samples with single labels, and as the assumption that the observed cloud
348 type occurs on such scales would likely not hold. The losses relative to the vision transformer models trained on the different
349 input tile sizes are detailed in Figure B.2. Since these models were trained on a reduced dataset as mentioned previously, their
350 skill cannot be directly compared to the one displayed in Figure 3. While the contrastive losses are similar across input tile sizes,
351 the reconstruction losses differ. Since we kept the ratio between the patch size and the tile size constant when training the
352 different models, the difference in reconstruction skill could be attributed to the dimensionality of each patch being much
353 smaller, for example for a tile of size 16x16 a patch will be 2x2. The reconstruction head being a fairly shallow CNN, the
354 reconstruction of the spatial patterns inside the patches showcases better skill for smaller input patches after a few epochs, while
355 for larger patch sizes - and thus tile sizes - a longer training process would be needed as to improve the truthfulness of the
356 reconstruction to the input. Examples of reconstructions depending on the input tile size are included in Figure B.3 and visually
357 display how a larger field of view can help capture the larger cloud organisation or even individual sparse clouds. To further
358 evaluate the potential benefit of the spatial context for the downstream classification task, we consider as an alternate input the
359 flattened cloud properties of a 9x9 tile centred on the observation location. This yields an input of similar dimensionality
360 compared to the latent space representation of both the CNN and the vision transformer (3 channels x 9 x 9 = 243). We then train
361 the same RF classification model on each of the latent representations derived from the trained vision transformers and on the
362 flattened cloud properties. From the classification metrics, we observe that the smaller the tile size the more prone the model is to
363 overfitting towards the majority classes (high and stratiform cloud types in the case of 4 types) leading to a decreased
364 performance on the validation set. For instance, choosing an input tile size of 16x16 results in a decrease of 20% across metrics
365 from the training to the validation set (compared to around 10-15% across metrics for the larger input tile sizes), and leads to
366 metrics on the validation set more than 10% lower than with larger input tile sizes. The predictions made using larger spatial
367 context (tile size greater than 16x16) outperform the method with 9x9 flattened tile inputs across all considered metrics on the
368 validation set. With the input tile size 16x16, the reduced spatial context seems to be limiting for the performance but another
369 explanation could be a complex latent space compared to the input dimensionality. Overall, even with the vision transformer
370 backbones being trained only partially, the wider input tile size provides better classification skill and generalisation to unseen
371 data. In the rest of the study and experiments, if not mentioned specifically, the input tile size is chosen to be 128x128.

3.3.2 Spatial generalisation

374 To investigate the spatial generalisation skill of the cloud classification method, we split our colocated dataset into samples
375 located in the Northern or Southern hemispheres. Two vision transformer models are additionally trained on samples from only
376 the respective hemisphere and tested on the other one. The losses relative to the training and testing of both hemispherical
377 models are included in Figure B.4. Both hemispherical models display similar performance both on the training and testing
378 datasets, showing that even for a reduced number of training samples, epochs and spatial coverage the vision transformer
379 architecture generalises well to unseen data. Building on the two trained vision transformers, we set out to evaluate the skill on
380 the classification tasks. Splitting the labels between the two hemispheres yields 9246 samples for the Northern hemisphere and
381 1848 samples for the Southern hemisphere. Investigating the different classification metrics for training and testing on both
382 hemispheres, it is clear that the classification model trained on the Southern hemisphere struggles to generalise from such a low
383 number of labelled samples and probably overfits since the performance is worsened on the Northern hemisphere samples
384 (decrease of almost 50% across metrics from the training to the testing set). The classification model trained on the Northern
385 hemisphere generalises well in the case of the 4 cloud types with consistent metric values between hemispheres (marginal
386 decrease of around 15% across metrics from the training to the testing set). Overall, the model trained on samples from the

387 Northern hemisphere and for both cases of number of cloud types, the performance on the Southern hemisphere is similar to
388 models with larger tile sizes from the previous section, showing consistency across experiments even with limited datasets for
389 the training of the vision transformer.
390

3.3.3 Balanced training dataset

391
392 Balancing the number of samples among classes in the input dataset can be a way to leverage enough information from the
393 underrepresented classes. We compare here the performance skill of two classification models trained on the colocated dataset or
394 on a balanced equivalent. To this extent, we use a sampler implementation from the *imbalanced-learn* package (Lemaitre et al.,
395 2017), namely the Synthetic Minority Oversampling Technique (SMOTE; Chawla et al., 2002) to oversample the minority
396 classes. Doing so leads to improved classification skill with consistent increases across metrics on the validation set of 3-7% and
397 15-35% for the cases of 4 or 10 cloud types, respectively. The oversampling impacts mostly the cloud types from the high and
398 medium classes, and from the cirrocumulus and cirrostratus classes, in the case of 4 cloud types and 10 cloud types, respectively
399 (see Table A.1). The methods evaluated in the following section will thus include the same over-sampling strategy to overcome
400 the representation of the minority classes and improve the performance on the classification task.

4 Evaluation

401
402

4.1 Classification evaluation

403
404
405 In the following section, we detail the classification performance on the test set of the previously mentioned models. Two
406 baseline models are included, namely a classification model built on the CNN autoencoder from Lenhardt et al. (2024a) and a RF
407 model built on the flattened 9x9 input tiles as described in section 3.3.1. The method developed in this study is represented by
408 two models using the aforementioned vision transformer model (see section 3.2) as backbone complemented by either a RF
409 classifier or a MLP (see section 3.3). In the rest of the study, we denote the trained vision transformer model followed by the
410 classification model as CloudViT (Cloud Vision Transformer) in its two classification variants (RF or MLP). The classification
411 metrics on the test dataset for these four models are summarised in Table 2 for the case of the 4 cloud types and in Table C.1 for
412 the 10 cloud types. Since the number of samples is very limited, the performance of the models cannot be only considered as is
413 but is further evaluated in the subsequent sections through distributions of cloud properties and spatial occurrence distributions.
414 The CloudVit/RF method performs the best across all of the three metrics included. Firstly, the macro-averaged multi-class
415 accuracy does not differ by a large margin between the different methods, but the class-wise accuracies reveal several limitations.
416 The baseline 9x9 RF model largely overfits towards the high and stratiform types (train and test class accuracies of 0.84/0.81 and
417 0.63/0.62, respectively), performing poorly on the medium and cumuliform types (train and test class accuracies of 0.31/0.21 and
418 0.19/0.15, respectively). The CloudViT/MLP model is biased towards stratiform clouds (train and test class accuracy of
419 0.79/0.79) while struggling to identify the other three types (train and test accuracies all falling between 0.10 and 0.40). The
420 baseline CNN/RF and the CloudViT/RF models are performing quite similarly both on aggregated and class-wise metrics.
421 However, the CloudViT/RF model showcases improved performance on the stratiform class (increase of 0.13 in the class
422 accuracy both on the train and test datasets) and only a marginal decrease (0.03) on the class accuracies for medium and
423 cumuliform clouds. The performance on the high clouds is similar with slightly higher accuracies for the CloudViT/RF model.
424 Other metrics like the IBA of the geometric mean and the F1-score further emphasise that the CloudViT/RF model outperforms
425 the other methods while addressing the imbalance training data to generalise with satisfactory skill on the unseen test dataset.
426 Furthermore, the patterns in the class accuracies can be traced back to shortcomings in the observational dataset. Having only
427 considered single-layer cloud scenes in the colocated dataset, the high clouds are well predicted in accordance with the
428 observations as a surface observer would identify with certainty this type of cloud if no other lower cloud is blocking the field of
429 view from the surface. Stratiform clouds could be more challenging for the observers as they typically display high cloud
430 fraction and high optical thickness, limiting the ability of the surface observer to quantify with certainty the amount of clouds in
431 other levels. However, such characteristics can be well captured by computer vision models which build on patterns in the
432 three-dimensional input data which in particular the baseline 9x9 RF model lacks. This difference between models is in particular
433 apparent for the cumuliform class which is mostly composed of observations of cumulus. A cloud scene relative to a cumulus
434 observation will most likely display a lower cloud fraction as the individual clouds are sparsely distributed, extracting only the
435 very near points around the observation might then be too reductive and limit the accuracy of the classification model. It is
436 confirmed by the accuracy on this cloud type for which the baseline 9x9 RF model is largely outperformed by all three other
437 models both on training and test datasets (class accuracy increases between 150% up to 260% on the test dataset).

438

Method	Multi-class accuracy *	IBA geometric mean	F1-score *
Baseline 9x9 RF	0.45	0.32	0.35
Baseline CNN/RF	0.45	0.32	0.40
CloudViT/MLP	0.40	0.32	0.42
CloudViT/RF	**0.46**	**0.36**	**0.43**
CloudViT/RF (train)	0.55	0.41	0.49

439 **Table 2: Classification metrics on the test set in the case of 4 cloud types. The metrics noted with a * are referring to their**
440 **macro-averaged estimate. The method on which the rest of the study is based is highlighted in bold. The baseline**
441 **CNN/RF refers to the CNN backbone introduced in Lenhardt et al. (2024a).**

442

443 **4.2 Histograms of cloud properties**

444

445 In order to evaluate the physical soundness of the predictions made by the CloudViT model, we investigate the distribution of
446 several cloud properties with respect to the observed and predicted cloud types. In Figure 5, we summarise the distribution of
447 cloud top pressure (CTP), cloud top height (CTH), cloud top temperature (CTT), cloud optical thickness (COT), cloud water path
448 (CWP) and cloud fraction (CF) for the 4 cloud types (high, medium, cumuliform, stratiform) and for three different datasets: the
449 test set labels, the test set predictions and the dataset of global predictions. The latter is built on global MODIS AQUA granules
450 for the year 2016 - the year is chosen to avoid any overlap with cloud scenes seen during the training of the vision transformer on
451 data from 2008 - from which we regularly sample tiles in order to build a more comprehensive and global dataset of cloud types
452 to further evaluate the method. The spatial distribution of cloud types for this dataset is highlighted in the following section and
453 the global dataset is made available at Lenhardt et al. (2024b). The histograms are built by reporting the respective cloud
454 properties for all the cloudy pixels in each sampled tile from the dataset apart from the cloud fraction which is computed for the
455 whole tile from the cloud mask. As a consequence, unless the whole cloud field is composed of only a single cloud type, the
456 histograms will cover a large range of cloud properties due to multi-layer clouds or multi cloud types scenes (e.g. convective
457 cells with associated anvils or cumulus/stratocumulus transitions). On Figure 5, the histograms pertaining to the test set labels
458 and predictions have distributions close to identical across cloud types showing a good agreement in the clouds depicted in both
459 datasets while the global dataset histograms provides a less noisy overview of the distribution of the cloud properties per cloud
460 type. The high clouds are characterised by low cloud water path and optical thickness, along with colder and higher cloud tops as
461 well as more frequent cloud fractions smaller than one. All of these aspects are emphasised in the global predictions compared to
462 the limited test set samples, showing the CloudViT model manages to extract the representative characteristics of the cloud type
463 from the labels. The cumuliform category encompasses mostly low warm clouds with reduced cloud fractions and moderate
464 cloud water path and optical thickness. Inside this class, the higher and colder cloud tops are concentrated in the cumulonimbus
465 class, along with larger cloud water path and cloud optical thickness (see Fig. C.1). The stratiform class includes thick cloud
466 fields with high cloud water path and almost full spatial coverage of the cloud scenes (cloud fraction close to 1 in most cases). A
467 fraction of the clouds in this class are slightly higher and colder and correspond to stratus/nimbostratus clouds which can also be
468 seen in Figure C.1. The distributions for medium clouds showcase similarities with several other types and are best evaluated in
469 combination with their spatial distribution (see Section 5). Examining in more detail the refined cloud types with the 10 cloud
470 types (see Fig. C.1) reveals slight differences inside broader cloud types. For example, the distinction between the three high
471 cloud types (cirrus, cirrostratus and cirrocumulus) appears through separations in cloud fraction, cloud optical thickness and
472 cloud water path which were not obvious from the limited amount of labelled samples. The differences between the three high
473 cloud types further manifest in distributions of cloud top quantities for which cirrus and cirrostratus display potential
474 multilayered cloud scenes with a combination of low/warm and high/cold cloud tops. Overall, the CloudViT model manages to
475 generalise well from a few samples (only around 10 for the cirrocumulus class) while ensuring physical consistency inside types.
476 Due to the large cloud scenes considered as input for the classification, the distribution of the cloud properties might not be as
477 representative of single cloud types as an input tile of, for example, 16 km. The main caveat regarding performance on high and
478 medium clouds from our method is that the ground-based observer identifies these cloud types with higher uncertainty compared
479 to that of low clouds. Additionally, stratiform clouds with high cloud fraction can hinder the trustworthiness of the surface

480 observation if the whole field of view is cloudy. Even though the limitations of ground-based observations are evident, they still
481 provide quality observations on which an efficient and skilled classification model can be trained.
482

483
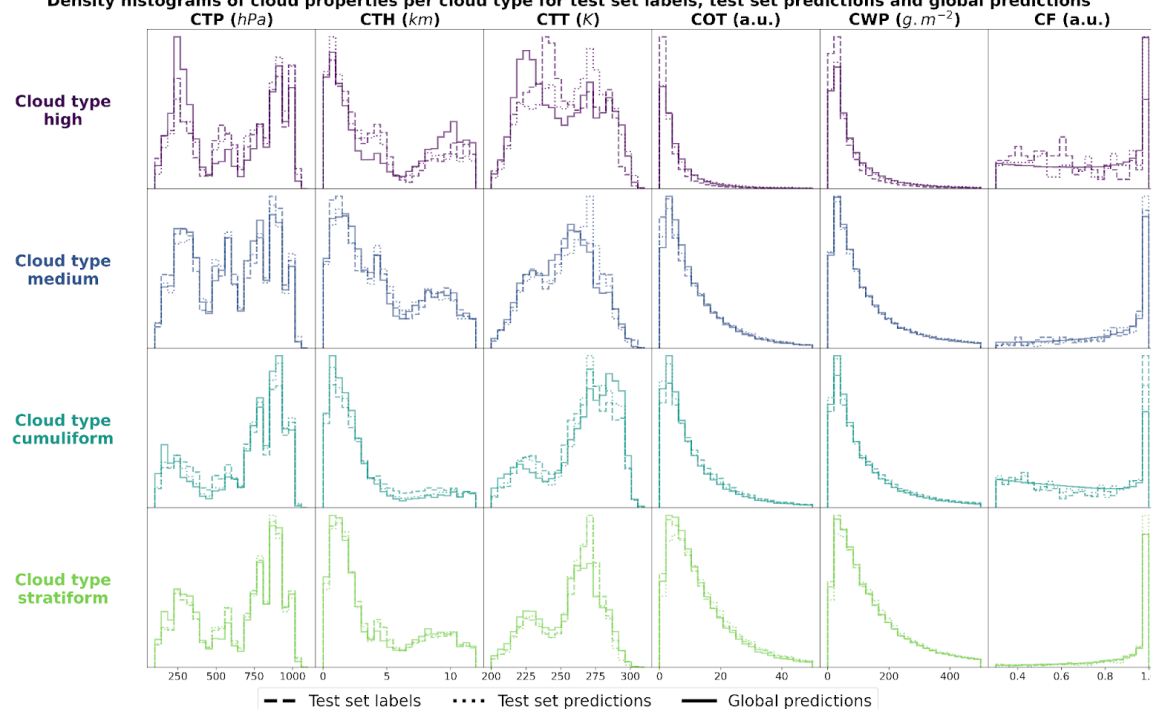
Figure 5: Density histograms of cloud properties for each cloud type from high, medium, cumuliform and stratiform.

5 Results

5.1 Global cloud type distributions in MODIS data

489 Additionally to the physical and microphysical characteristics of the different cloud types, their global spatial distribution can
490 help us further understand in which regions they are more or less frequent and qualitatively assess the presented classification
491 method compared to other remote sensing products. To this extent, as mentioned in the previous evaluation section (see Section
492 4), we build an extensive cloud type dataset for the year 2016 from MODIS AQUA granules which are regularly sampled for
493 tiles of 128x128 pixels. The sampling step (64) is chosen for computational efficiency and memory purposes to be not too small
494 to avoid large overlap between neighbouring tiles but large enough to ensure representativeness in the later aggregated
495 predictions of the MODIS granules. Furthermore, as the area covered by each tile is rather wide, the spatial distribution of cloud
496 types might be less smooth than other products (e.g. Sassen et al., 2008) or other methods (Zantedeschi et al., 2020) which are
497 providing cloud types for smaller cloud fields. Additionally, the dataset is built on single daily overpasses of the MODIS
498 instrument and can thus be biassed towards the local retrieval time (13:30 h , early afternoon for AQUA).
499 The spatial distributions of the predicted cloud types for the global dataset for the year 2016 are detailed in Figure 6 and Figure
500 C.2 for 4 and 10 cloud types, respectively. Firstly, we note that CloudViT predictions capture large scale patterns which are in
501 agreement with observational datasets (Sassen et al., 2008; Cesana et al., 2019; Wood, 2012; Pincus et al., 2023). Stratiform
502 clouds, and in particular stratocumulus (see Fig C.2), are frequent in the high latitudes and along the western coasts of America
503 and Africa. Cumuliform clouds are concentrated in the Tropics apart from the areas where stratocumulus clouds are dominant.
504 Medium clouds are concentrated in the polar regions and over land in the higher latitudes. High clouds make up a large portion
505 of clouds in the polar regions but also over land. The first notable difference is the low occurrence of high clouds in the Tropics
506 which would be expected to be higher (Sassen et al., 2008; Pincus et al., 2023). An explanation could be the frequent occurrence

507 of high clouds in multi-layer cloud scenes related to convection in the Tropics. Furthermore, in such cases the model probably
508 identifies the cloud types with larger cloud fraction and thus discards potential high clouds in the scene. Incorporating more
509 samples of high clouds in that region (see Fig. A.1) could potentially help the performance of the classification model in that
510 regard.
511
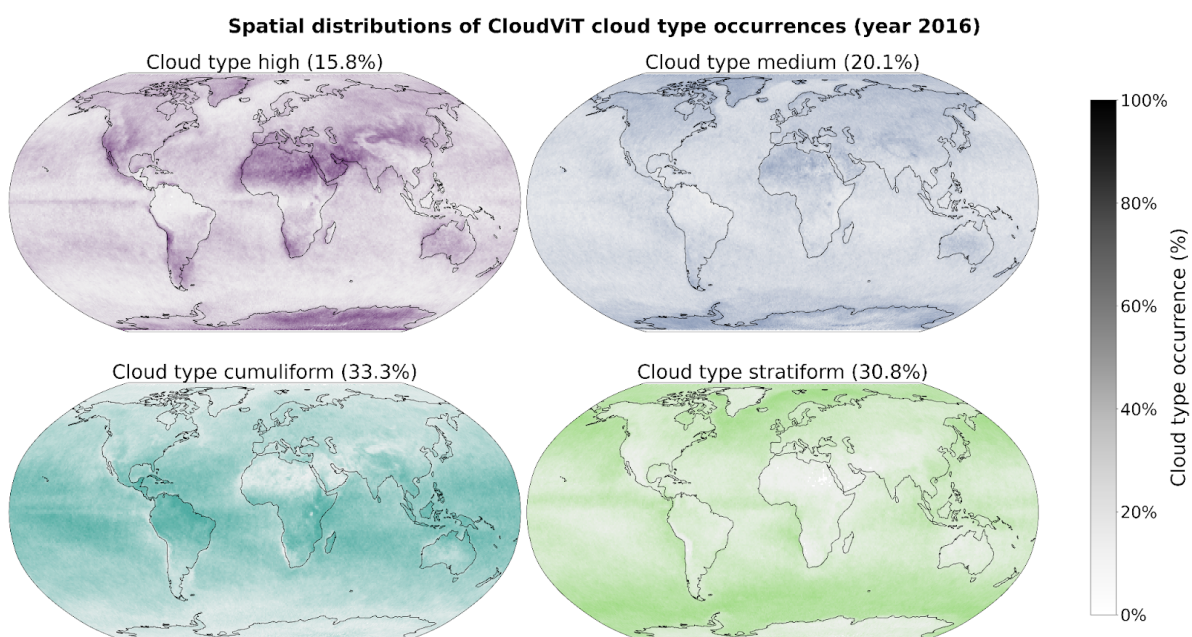
512
513 **Figure 6: Spatial distributions of the CloudViT cloud type occurrences (cloud types high, medium, cumuliform,**
514 **stratiform) for MYD06 granules for the year 2016 aggregated on a 1° regular grid.**
515
516 **5.2 Application to a global strom-resolving model simulation**
517

518 As a proof of concept, we investigate the cloud type representation in general circulation model (GCM) outputs using our
519 CloudViT method. We build on a new generation of GCMs at kilometre resolution, namely the ICON-Sapphire (Hohenegger et
520 al., 2023). As the resolution of the simulation increases, some processes like deep convection can be directly resolved instead of
521 parameterized. Hence, building diagnostics about cloud representation is of importance to help evaluate the simulations. In
522 particular, we use the simulation run by the Max Planck Institute for Meteorology (MPI-M) for the period between the 5th and
523 12th of December 1972, aiming at recreating the Blue Marble picture made during the Apollo 17 mission on the 7th of
524 December. Here we only use the complete outputs provided for the 11th of December. The grid used contains 335 544 320 grid
525 points at each level in the atmosphere (R02B11 grid), and outputs are provided every 30 minutes during the simulation for the
526 atmospheric quantities of interest, resulting in overall 48 time steps. As the effective horizontal resolution of the model
527 simulation and the MODIS data are on similar scales, we can effectively apply CloudViT on the model outputs. From the model
528 outputs, we derive the cloud properties necessary for the method introduced in this study. More information about the particular
529 model setup and the derivation of cloud properties is included in Appendix D. However, the standardisation of the input cloud
530 properties for the vision transformer model is still done based on statistics computed on MODIS data which could induce a bias
531 in the latent representations and subsequently on the predictions. Extending the method to other datasets like this GCM
532 simulation thus requires careful investigation that the cloud properties lie in the same range or display similar distributions.
533 For each 30-minute time step, we proceed to sample tiles, regularly spaced, to reach global coverage of cloud type retrievals.
534 Figure 7 displays the daily averaged occurrence of the cloud type predictions on a 1° regular grid for the 4 cloud types, the
535 equivalent for 10 cloud types is presented in Figure D.3. A large proportion of the predicted clouds belong to the high cloud type,
536 hinting at the difference in sensitivity to clouds retrieved in the climate model data compared to the MODIS retrievals. However,
537 increasing the cloud ice content threshold by an order of magnitude greatly decreases the amount of thin, high and cold clouds in

538 the simulation dataset. This aspect would need further tuning through comparison with remote sensing retrievals which are not
539 available for this particular simulated period. On the other hand, the cumuliform class captures well the convective systems in the
540 tropics while the stratocumulus decks can be identified (Fig. D.3). Additionally, the medium clouds are more present at high
541 latitudes. An important aspect to factor in is that the classification model was only trained on daytime satellite observations as the
542 optical cloud properties necessary are only available then. Thus, results on nighttime cloud retrievals which is the case for some
543 of the predictions produced from the presented simulation might need more meticulous evaluation. Even though it is a limiting
544 factor in the case of the satellite dataset we are using, the simulation outputs provide us with the required variables across all
545 timesteps.
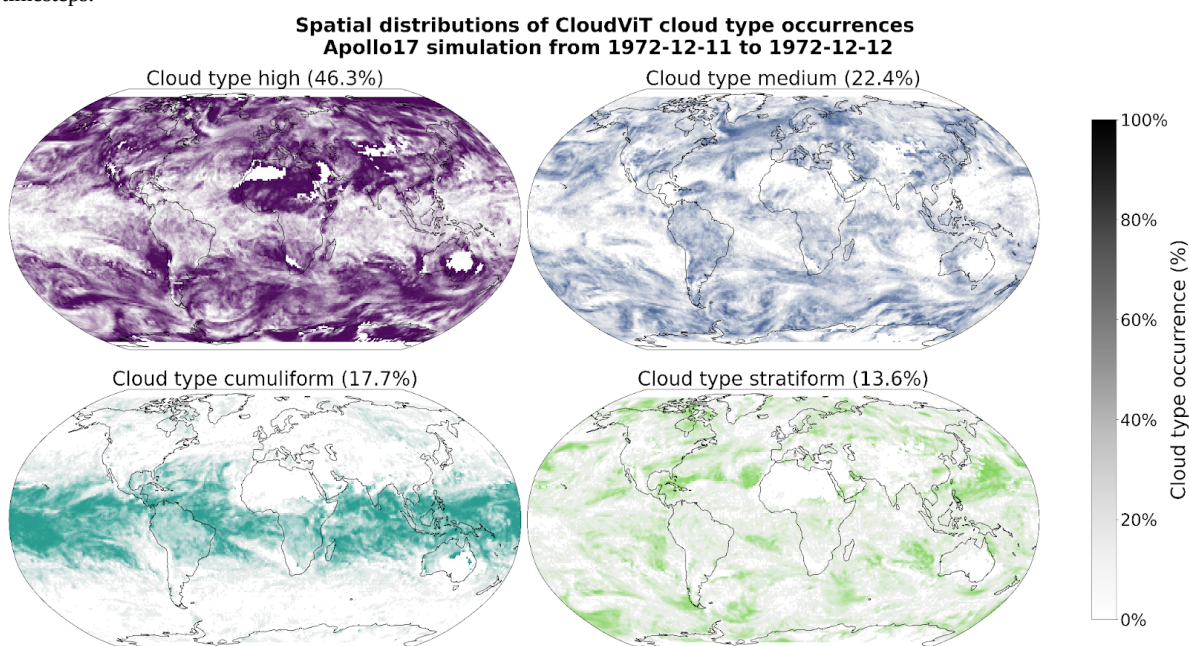
546
547 **Figure 7: Spatial distributions of the CloudViT cloud type occurrences (cloud types high, medium, cumuliform,**
548 **stratiform) for the ICON-Sapphire Apollo 17 simulation of December 11th 1972 aggregated on a 1° regular grid.**

549 **6 Conclusion**
550
551 This study introduces a new method called CloudViT to classify cloud types from MODIS cloud properties, specifically CTH,
552 COT and CWP. CloudViT delivers robust cloud classification estimates for either 4 (high, medium, cumuliform, stratiform) or 10
553 (cirrus, cirrostratus, cirrocumulus, altostratus, altocumulus, cumulus, cumulus and stratocumulus, cumulonimbus, stratocumulus,
554 stratus) cloud types. The classification model was built on ground-based observations of cloud types (Section 2.1) and
555 experiments about its generalisation skill and the benefits of spatial information were presented (Section 3). We evaluated the
556 classification model by examining distributions of cloud properties in Section 4 and the global spatial distribution of cloud types
557 in Section 5.1. Lastly, we transferred our method to a km-scale climate model simulation made with ICON-Sapphire (Section
558 5.2). The global dataset alongside the CloudViT code and weights are made available on Zenodo (Lenhardt et al., 2024b).
559 Spatially-resolved cloud properties provide usable context for the CloudViT model to improve the cloud classification, as shown
560 in the comparison to the baseline method with limited spatial information. Introducing this new transformer model architecture
561 additionally improves the classification skill over the CNN backbone mentioned in Lenhardt et al. (2024a). Overall, CloudViT
562 achieves acceptable performance even on sparsely represented classes for both cases of 4 and 10 cloud types. The limited
563 colocated dataset proves to be a hurdle for the proper evaluation of the method on labelled samples but the generation of an
564 extensive global dataset allows deeper investigation into the cloud types. In this dataset, the predicted cloud types exhibit
565 physically reasonable distributions of their respective cloud properties, and their global spatial distributions are consistent with
566 other products (Section 5.1). Application to climate model data proves to be straightforward and results in insights into how

clouds are represented in global km-scale simulations. The necessary cloud quantities are obtained from common simulation outputs (cloud liquid water and ice contents, altitude, droplet number) which makes CloudViT easily applicable to other climate model simulations. Cloud type diagnostics such as CloudViT can be a resourceful addition to the panel of assessment methods for model data (Kuma et al., 2023; Kaps et al., 2023).

Overall, the method would benefit from including further ground-based observations through the colocation process but then much larger storage and computational facilities would be needed as global MODIS data represents thousands of granules each day. The classification model could also be refined by finding better alternatives to the RF or MLP presented here. The overall finetuning process involving the vision transformer and the MLP classification head proved to be cumbersome but holds great promise if the labels and training process are refined. Transfer learning from a typical ImageNet-trained model did not yield a notable performance difference which shows the current need for foundation models trained on remote sensing data. The main hurdle here remains the large diversity in instruments, quantities and resolutions among remote sensing products which hinders the possibility of a unified model.

To improve the spatial coverage of the CloudViT predictions, the direct application to granules from MODIS TERRA would technically not require much more work as the instruments are similar and provide the same cloud properties. An additional benefit would come after the upcoming decommissioning of the CloudSat mission which was providing cloud type retrievals along its track aligned with MODIS. We would then be able to still offer information about cloud types over the same areas even though no vertical information is available and used from our predictions on MODIS level 2 data. As for other satellite cloud products, the main difference would arise, similarly to climate model data, from the potentially different distributions and ranges in the input cloud properties which would need either retraining of the vision transformer or careful scaling to match the distributions seen in MODIS data.

Furthermore, some caveats appear when applying CloudViT to climate model data. As mentioned previously, the input scaling is crucial to ensure proper portability of the method to this other data source. The absence of nighttime retrievals in the MODIS data also turns the evaluation of predictions on nighttime data points across the model data into a challenging issue. However, clouds play a role in the climate system both during the day when they cool the surface by mostly reflecting incoming solar radiation but also at night when they warm the surface by trapping outgoing terrestrial radiation. Shifts and changes in cloud occurrence and distribution in the current climate but also in future projections could further influence global climate change (Luo et al., 2024). The proof of concept in applying CloudViT to a limited climate model simulation is encouraging but considering more common and computationally less expensive global km-scale simulations (horizontal resolution of 5 km for example) could be of greater interest to the community to study longer time scales. To this extent, two conceivable approaches would consist in either retraining the CloudViT model on coarser input cloud properties matching the model data resolution - the MODIS Cloud product is also available at a 5 km resolution even though the 1 km equivalent is recommended for use - or in using CloudViT as is but with the coarse input scaled to fit the resolution of the tiles on which it was trained on. The first option could be more interesting as computer vision models are commonly trained on coarser resolutions first to learn the broad specificity and patterns in the data before fine-tuning the model on finer resolution (Touvron et al., 2019).

601 **Appendix**

602 **Appendix A: Cloud type observations**

WMO codes	Cloud type: 4 groups	Cloud type: 10 groups	Colocated samples
High clouds 1-6	High	Cirrus	n = 574
High clouds 7-8		Cirrostratus	n = 142
High clouds 9		Cirrocumulus	n = 29
Medium clouds 1-2	Medium	Altostratus	n = 420
Medium clouds 3-9		Altocumulus	n = 944
Low clouds 1-3	Cumuliform	Cumulus	n = 1998
Low clouds 8		Cumulus and stratocumulus	n = 533
Low clouds 9		Cumulonimbus	n = 519
Low clouds 4-5	Stratiform	Stratocumulus	n = 2274
Low clouds 6-7		Stratus	n = 3661

603 **Table A.1: Cloud types from the WMO observational datasets, their groups following Kuma et al. (2023) and the**
604 **corresponding number of samples in the colocated dataset. The WMO codes correspond to the 9 types for each level.**

605
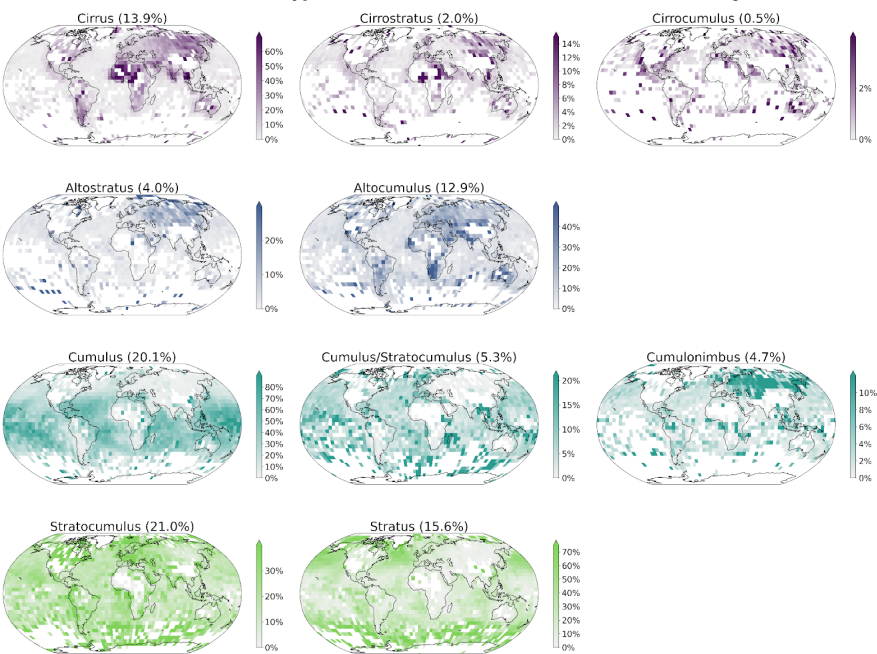
606 **Figure A.1: Spatial distributions of observed cloud types (cloud types cirrus, cirrostratus, cirrocumulus, altostratus,**
607 **altocumulus, cumulus, cumulus and stratocumulus, cumulonimbus, stratocumulus, stratus) from the Met Office datasets**
608 **(Met Office, 2006; Met Office, 2008) for the years 2008 and 2016. Overall percentage of each label in the total dataset is**
609 **indicated in brackets.**
610

611
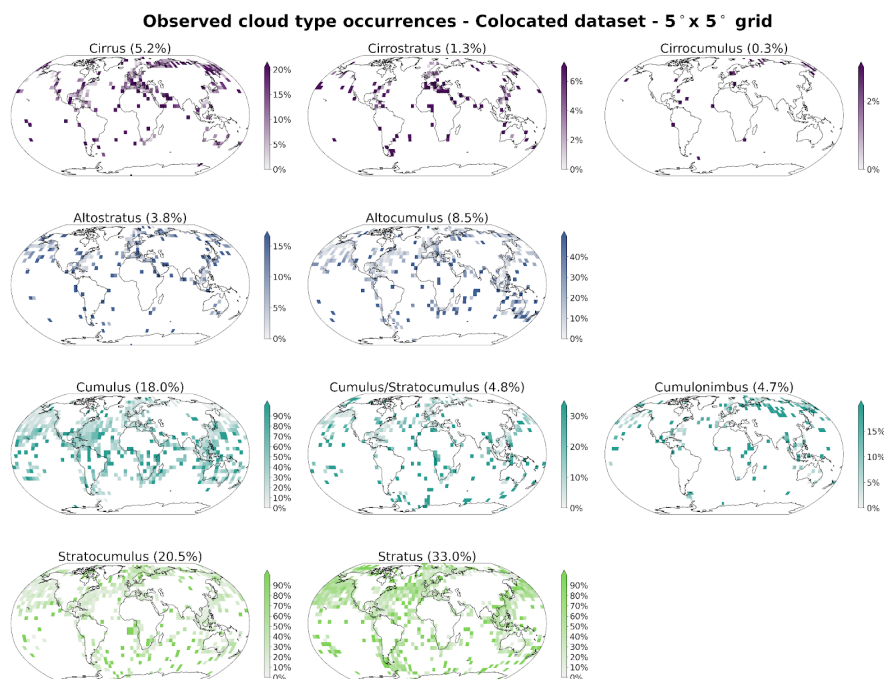
Figure A.2: Spatial distributions of observed cloud types (cloud types cirrus, cirrostratus, cirrocumulus, altostratus,
altocumulus, cumulus, cumulus and stratocumulus, cumulonimbus, stratocumulus, stratus) from the Met Office datasets
(Met Office, 2006; Met Office, 2008) for the years 2008 and 2016 colocated with the satellite cloud retrievals (Platnick et
al., 2017) used for training the classification model. Overall percentage of each label in the total dataset is indicated in
brackets.

Appendix B : Vision transformer training and sensitivity on the cloud classification task

B.1 Model architecture and pretrained weights
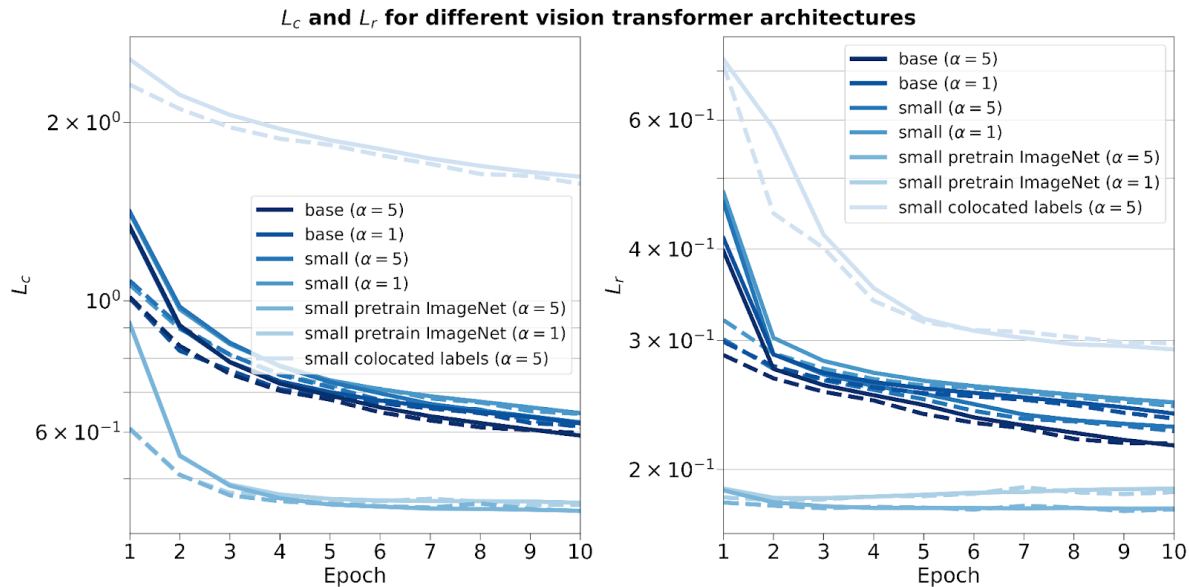
Figure B.1: Training and validation contrastive (left) and reconstruction (right) losses for different vision transformer architectures, pretraining weights, training datasets and scaling factor α.

B.2 Reconstruction errors for the CNN autoencoder and the vision transformer (small variant) on the test set

Model type	Reconstruction error	CTH	COT	CWP
CNN autoencoder	MSE	0.27	0.39	0.25
	l1-loss	0.36	0.33	0.21
Vision transformer (small variant)	MSE	0.06	0.25	0.13
	l1-loss	0.10	0.17	0.10

Table B.1: Reconstruction relative errors of the CNN (Lenhardt et al., 2024a) and the vision transformer models across channels (CTH, COT and CWP) on the test dataset.

B.3 Spatial context and input tile size
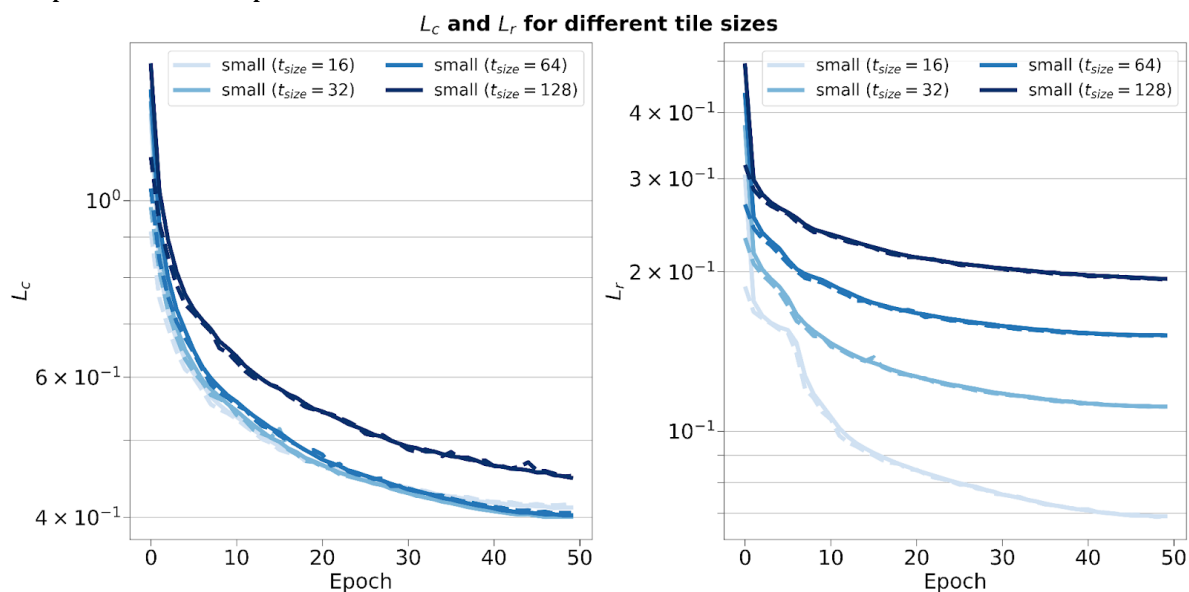
Figure B.2: Training and validation contrastive (left) and reconstruction (right) losses for vision transformers trained on different input tile sizes of 16, 32, 64 and 128.
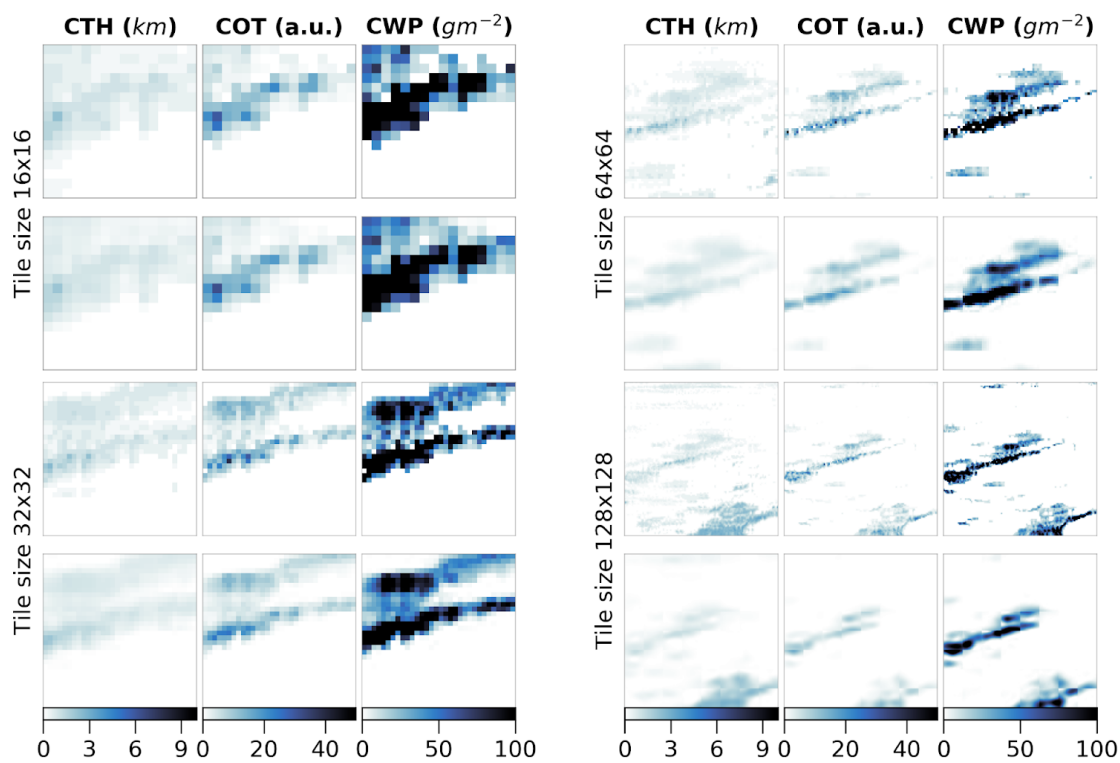
Figure B.3: Input tiles (first and third rows) and corresponding reconstructions (second and fourth rows) for vision transformers trained on the relevant input tile sizes of 16, 32, 64 and 128.

B.4 Spatial generalisation
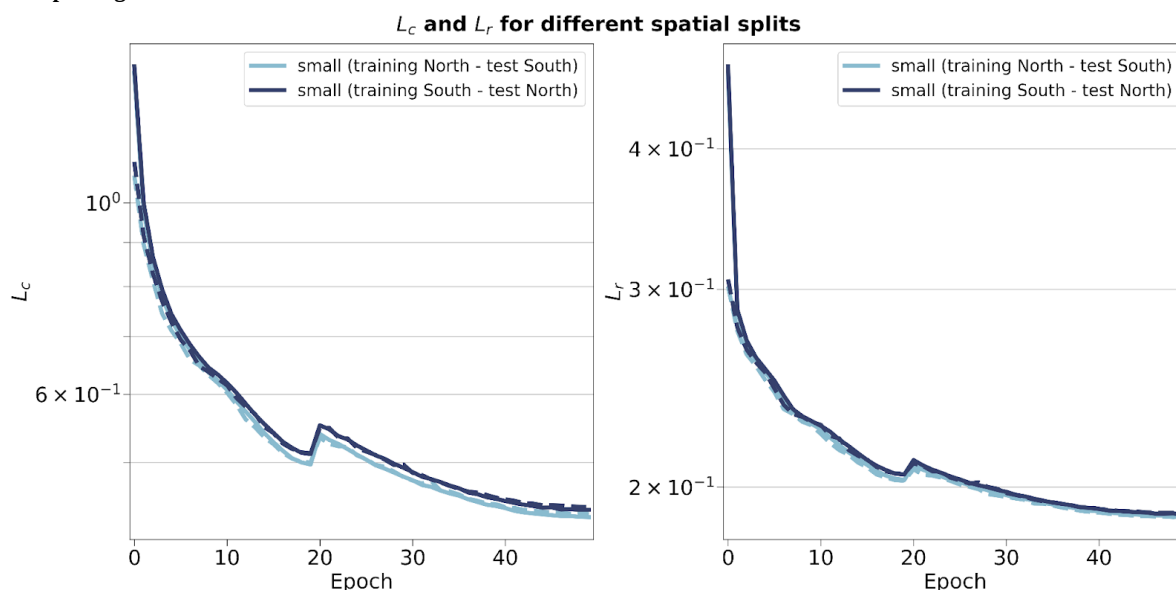
Figure B.4: Training (full lines) and validation (dashed lines) metrics for the contrastive (left) and reconstruction (right) losses for vision transformers trained on samples from the Northern or Southern hemispheres.
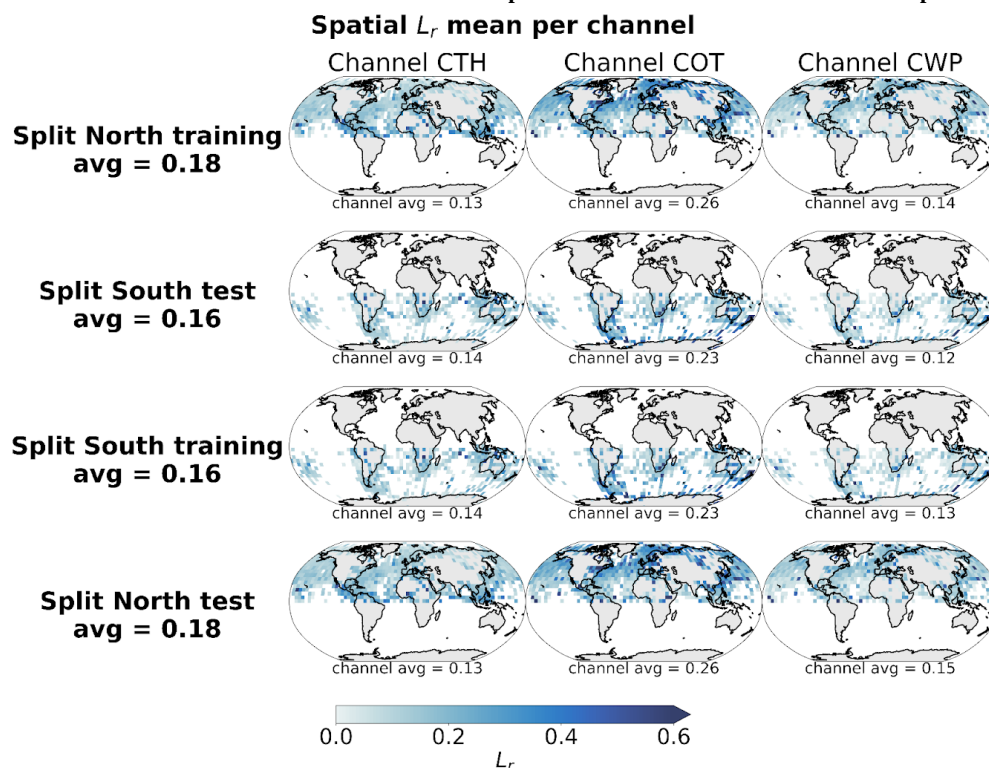
Figure B.5: Spatial distributions of the mean channel reconstruction errors for the Northern and Southern hemispheres colocated samples. The first two rows correspond to the model trained on the samples from the Northern hemisphere and the last two rows to the model trained on the samples from the Southern hemisphere.

Appendix C: Cloud type classification for 10 types

Method	Multi-class accuracy *	IBA geometric mean	F1-score *
Baseline 9x9 RF	0.19	0.26	0.16
Baseline CNN/RF	0.22	0.18	0.17
CloudViT/MLP	0.22	0.20	0.16
CloudViT/RF	**0.23**	**0.26**	**0.21**

Table C.1: Classification metrics on the test set in the case of 10 cloud types. The metrics noted with a * are referring to their macro-averaged estimate. The baseline CNN/RF refers to the CNN backbone introduced in Lenhardt et al. (2024a).
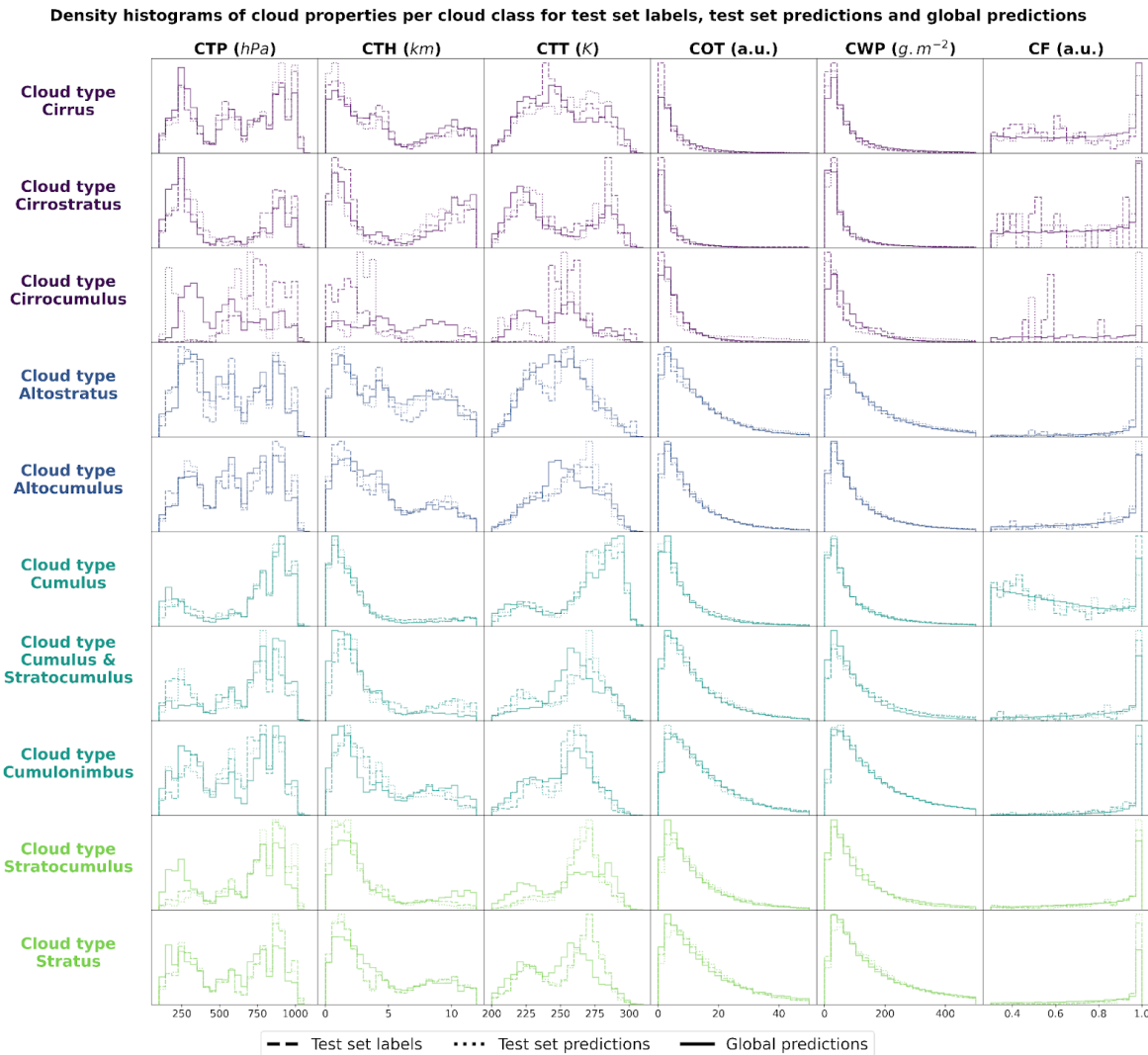
Figure C.1: Density histograms of cloud properties for each cloud type from cirrus, cirrostratus, cirrocumulus, altostratus, altocumulus, cumulus, cumulus and stratocumulus, cumulonimbus, stratocumulus, stratus.
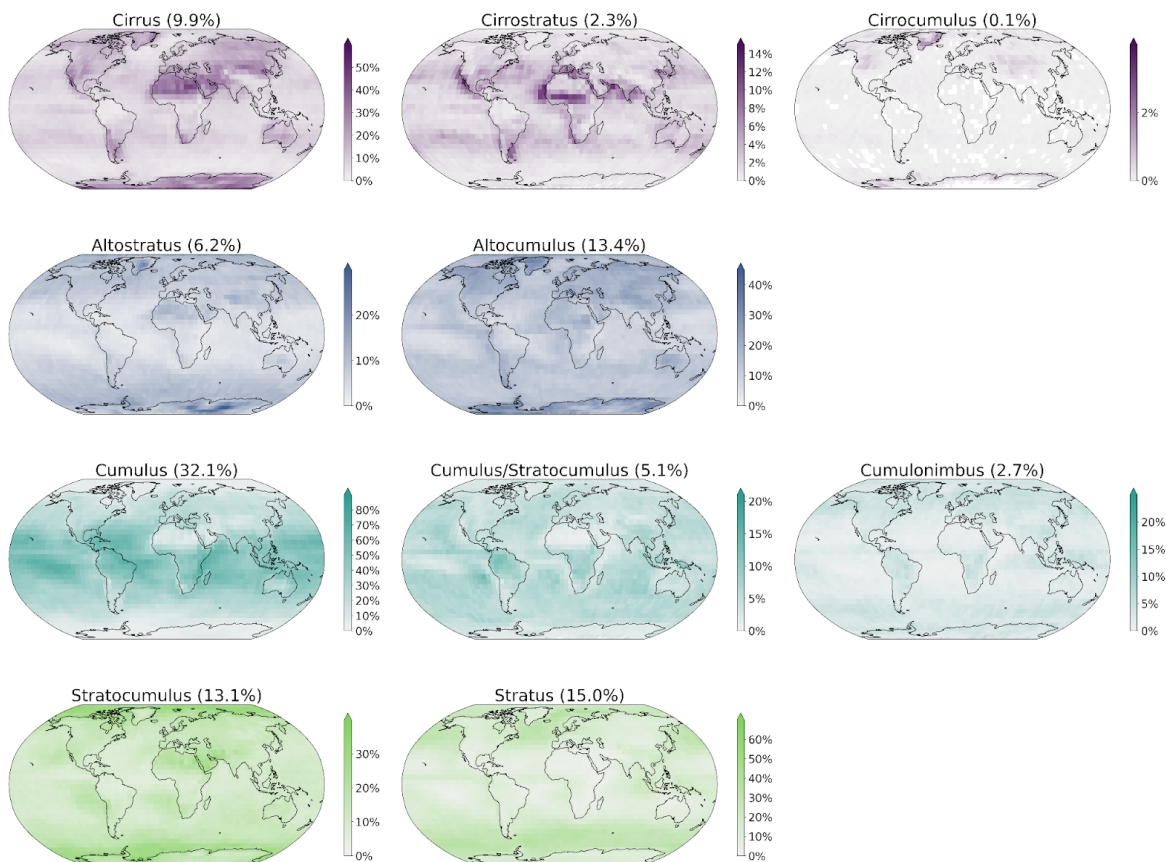
Figure C.2: Spatial distributions of the CloudViT cloud type occurrences (cloud types cirrus, cirrostratus, cirrocumulus, altostratus, altocumulus, cumulus, cumulus and stratocumulus, cumulonimbus, stratocumulus, stratus) for MYD06 granules for the year 2016 aggregated on a 1° regular grid.

Appendix D: Cloud properties computation from model simulation output

In order to compute the different cloud properties used in our method (Table 1), we use the available atmospheric outputs from the model simulation. The simulation was made using the ICON-2.6.6-rc version in R02B11 grid resolution with 90 vertical levels in the atmosphere (335544320 grid points per level) and 128 vertical levels in the ocean (237102291 surface grid points). Observed aerosols and greenhouse gas concentrations of December 1972 were used for the atmosphere.

The cloud top quantities are retrieved by defining the top-most level where the liquid water content (variable name *clw*) or the ice content (variable name *cli*) are above a predefined threshold of 1 mg.kg^{-1}. This threshold relates to particles of sizes of at least a few micrometres which is similar to what the sensors on the MODIS AQUA instrument are able to retrieve. Using 3D outputs of atmospheric quantities like temperature (variable name *ta*) and pressure (variable name *pfull*), we derive the cloud top properties also present in the MODIS MOD/MYD06 level 2 cloud properties product. The CTH is derived using the altitude in the corresponding vertical level in the grid. Secondly, the CWP is computed by summing the vertically integrated cloud liquid water path (variable name *cllvi*) and cloud ice path (variable name *clivi*) which are already provided as simulation outputs. Lastly, we computed the COT by vertically summing the layer-wise COT computed from the following equation, detailed in Carslaw (2022), equation 12.49 (Chapter 12.3, page 515):

$$\tau_c = \frac{9}{5}\left(\frac{4\pi}{3\sqrt{2}}\right)^{1/3}\rho_w^{-2/3}(kN_d)^{1/3}c_w^{-1/6}L^{5/6} = 0.2303\ kg^{-5/6}\ m^{8/3}\ (kN_d)^{1/3}\ L^{5/6} \qquad (D.1)$$

Where $L = clw * \rho_{air} * \delta z$ the layer liquid water path, $\rho_w = 1000$ kg.m^{-3} density of water, $k = 1$ a factor to account for the width of the droplet size distribution, $c_w = 2e^{-6}$ kg.m^{-4} the adiabatic condensation rate and N_d the vertical droplet number defined in the simulation by the ECHAM6 parameterization (Equation 6; Stevens et al., 2013).
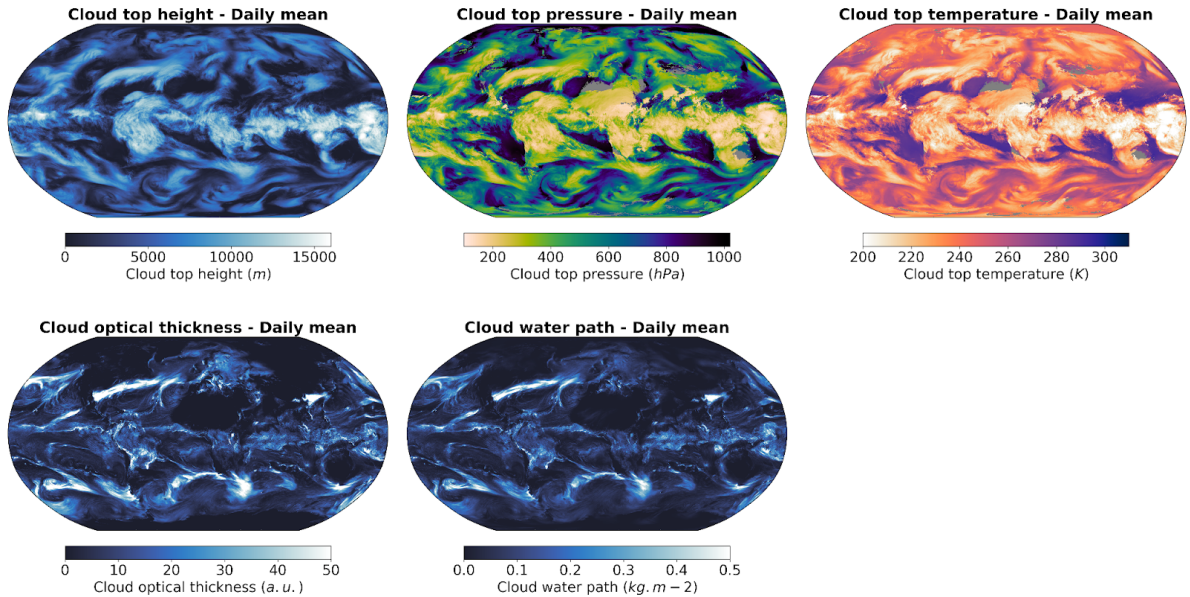
Figure D.1: Daily averages of cloud top height, cloud top pressure, cloud top temperature, cloud optical thickness and cloud water path for the 11th of December 1972 from the ICON-Sapphire Apollo 17 simulation.
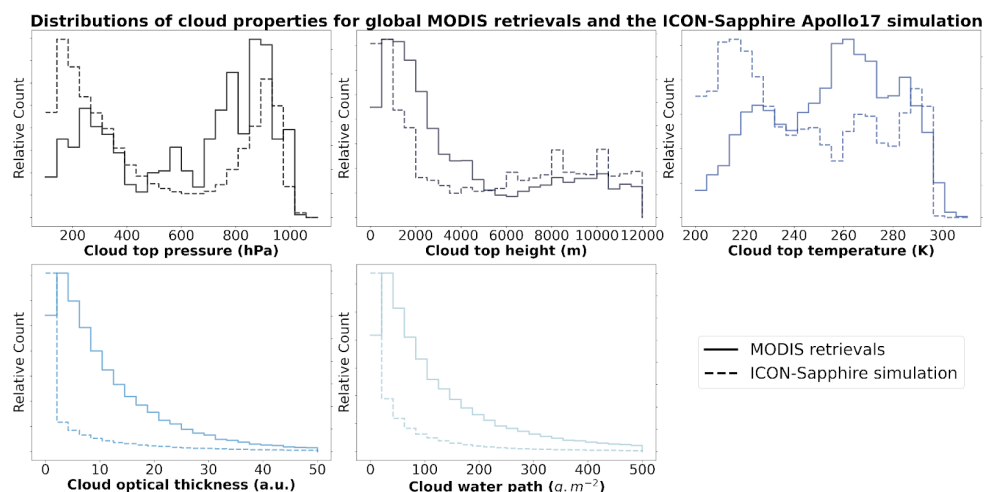
Figure D.2: Distribution of cloud top pressure, cloud top height, cloud top temperature, cloud optical thickness and cloud water path for MODIS AQUA retrievals and the ICON-Sapphire Apollo 17 simulation.
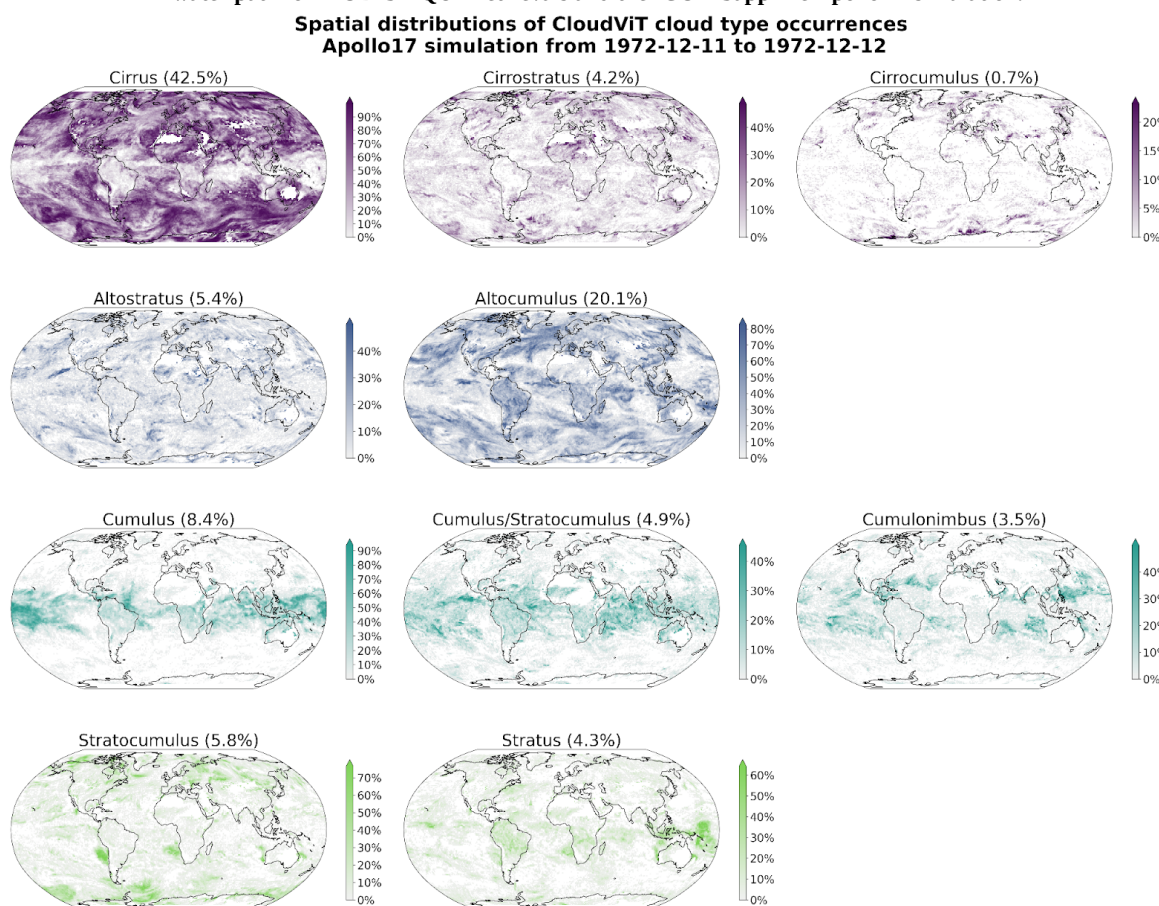
Figure D.3: Spatial distribution of the CloudViT cloud type occurrences (cloud types cirrus, cirrostratus, cirrocumulus, altostratus, altocumulus, cumulus, cumulus and stratocumulus, cumulonimbus, stratocumulus, stratus) for the ICON-Sapphire Apollo 17 simulation of December 11th 1972 aggregated on a 1° regular grid.

Code availability

The code used for the method and producing the plots is available on Zenodo (Lenhardt et al., 2024b).

Data availability

The global dataset of the cloud type predictions for the year 2016 is available on Zenodo (Lenhardt et al., 2024b). The dataset is available as a csv file with corresponding coordinates, MODIS granule file, time of retrieval and predicted cloud type (4 and 10 groups) or in a netCDF file as daily aggregates on a regular grid with a resolution of 1 ° or 5 °. The meteorological observations from the UK MetOffice (Met Office, 2006; Met Office 2008) are available through the CEDA archive at https://catalogue.ceda.ac.uk/uuid/77910bcec71c820d4c92f40d3ed3f249 and https://catalogue.ceda.ac.uk/uuid/9f80d42106ba708f92ada730ba321831 for ocean and land observations respectively. The files from the CUMULO dataset (Zantedeschi et al., 2019) are available at https://www.dropbox.com/sh/i3s9q2v2jjyk2it/AACxXnXfMF5wuIqLXqH4NJOra?dl=0. The simulation outputs are hosted by the DKRZ (Deutsches Klimarechenzentrum).

Author contribution

JL, JQ, DS and DK designed the study. JL wrote the code. DK provided support regarding the climate model data. JL conducted the analysis and JL, JQ and DS interpreted the results. JL prepared the manuscript, JQ, DS and DK reviewed the manuscript and provided comments.

Competing interests

Some authors are members of the editorial board of journal ACP.

Acknowledgements

This work was supported by the European Union's Horizon 2020 research and innovation programme under Marie Skłodowska-Curie grant agreement No. 860100 (iMIRACLI). We thank the Leipzig University Scientific Computing cluster and the DKRZ (Deutsches Klimarechenzentrum, projects number bb1036 and bb1153) for computing and data hosting. We acknowledge the contributors of the CUMULO dataset (Zantedeschi et al., 2019) for providing access to the data files hosted at https://www.dropbox.com/sh/i3s9q2v2jjyk2it/AACxXnXfMF5wuIqLXqH4NJOra?dl=0. Additionally, we acknowledge the MODIS L2 Cloud product data set from the Level-1 and Atmosphere Archive and Distribution System (LAADS) Distributed Active Archive Center (DAAC), located in the Goddard Space Flight Center in Greenbelt, Maryland (https://ladsweb.modaps.eosdis.nasa.gov/archive/allData/61/MYD06_L2/). We would like to also acknowledge Monika Esch, Emilie Fons and Hans Segura for support and discussions in handling the climate model data.

References

Ackerman, S. A., and Frey, R.: MODIS Atmosphere L2 Cloud Mask Product (35_L2), NASA MODIS Adaptive Processing System, Goddard Space Flight Center, http://doi.org/10.5067/MODIS/MOD35_L2.061, http://doi.org/10.5067/MODIS/MYD35_L2.061, 2017.

Atito, S., Awais, M., & Kittler, J.: Sit: Self-supervised vision transformer, arXiv preprint, https://doi.org/10.48550/arXiv.2104.03602, 2021.

Baum, B.A., Menzel, W. P., Frey, R. A., Tobin, D. C., Holz, R. E., Ackerman, S. A., Heidinger, A. K., and Yang, P.: MODIS Cloud-Top Property Refinements for Collection 6, Journal of Applied Meteorology and Climatology, 51, 6, 1145-1163, https://doi.org/10.1175/JAMC-D-11-0203.1, 2012.

Boucher, O., Randall, D., Artaxo, P., Bretherton, C., Feingold, G., Forster, P., Kerminen, V.-M., Kondo, Y., Liao, H., Lohmann, U., Rasch, P., Satheesh, S. K., Sherwood, S., Stevens, B. and Zhang, X. Y.: Clouds and aerosols, Climate Change 2013: The Physical Science Basis. Contribution of Working Group I to the Fifth Assessment Report of the Intergovernmental Panel on Climate Change, 571-657, https://doi.org/10.1017/CBO9781107415324.016, 2013.

Breiman, L.: Random Forests. Machine Learning, 45 (1), 5–32, https://doi.org/10.1023/A:1010933404324, 2001.

Carslaw, K.: Aerosols and Climate, 1st Edition, Elsevier, ISBN 9780128197660, 2022.

Cesana, G., Del Genio, A. D., and Chepfer, H.: The Cumulus And Stratocumulus CloudSat-CALIPSO Dataset (CASCCAD), Earth Syst. Sci. Data, 11, 1745–1764, https://doi.org/10.5194/essd-11-1745-2019, 2019.

Chawla, N. V., Bowyer, K. W., Hall, L. O., and Kegelmeyer, W. P.: Smote: synthetic minority over-sampling technique, Journal of artificial intelligence research, 16, 321–357, https://doi.org/10.1613/jair.953, 2002.

Chen, T., Kornblith, S., Norouzi, M., and Hinton, G.: A simple framework for contrastive learning of visual representations, in: Proceedings of the 37th International Conference on Machine Learning (ICML'20), Journal of Machine Learning Research, 119, 1597–1607, https://dl.acm.org/doi/10.5555/3524938.3525087, 2020.

Deng, J., Dong, W., Socher, R., Li, L., Li, K., and Fei-Fei, L.: Imagenet: A large-scale hierarchical image database, in: 2009 IEEE conference on computer vision and pattern recognition, Miami, FL, USA, 248–255, https://doi.org/10.1109/CVPR.2009.5206848, 2009.

Dosovitskiy, A., Beyer, L., Kolesnikov, A., Weissenborn, D., Zhai, X., Unterthiner, T., Dehghani, M., Minderer, M., Heigold, G., Gelly, S., Uszkoreit, J., and Houlsby, N. : An image is worth 16x16 words: Transformers for image recognition at scale, arXiv preprint, https://doi.org/10.48550/arXiv.2010.11929, 2020.

Forster, P., T. Storelvmo, K. Armour, W. Collins, J.-L. Dufresne, D. Frame, D.J. Lunt, T. Mauritsen, M.D. Palmer, M. Watanabe, M. Wild, and H. Zhang: The Earth's Energy Budget, Climate Feedbacks, and Climate Sensitivity, in Climate Change 2021: The Physical Science Basis. Contribution of Working Group I to the Sixth Assessment Report of the Intergovernmental Panel on Climate Change [Masson-Delmotte, V., P. Zhai, A. Pirani, S.L. Connors, C. Péan, S. Berger, N. Caud, Y. Chen, L. Goldfarb, M.I. Gomis, M. Huang, K. Leitzell, E. Lonnoy, J.B.R. Matthews, T.K. Maycock, T. Waterfield, O. Yelekçi, R. Yu, and B. Zhou (eds.)]. Cambridge University Press, Cambridge, United Kingdom and New York, NY, USA, pp. 923–1054, http://doi.org/10.1017/9781009157896.009, 2021.

García, V., Sánchez, J. S., and Mollineda, R. A.: On the effectiveness of preprocessing methods when dealing with different levels of class imbalance, Knowledge-Based Systems, 25, 13–21, https://doi.org/10.1016/j.knosys.2011.06.013, 2012.

776 Hendrycks, D., and Gimpel, K.: Gaussian error linear units (gelus), arXiv preprint, https://doi.org/10.48550/arXiv.1606.08415,
777 2016.
778
779 Hinton, G. E.: Connectionist learning procedures, Artificial intelligence, 40, 185-234,
780 https://doi.org/10.1016/0004-3702(89)90049-0, 1989.
781
782 Hohenegger, C., Korn, P., Linardakis, L., Redler, R., Schnur, R., Adamidis, P., Bao, J., Bastin, S., Behravesh, M., Bergemann,
783 M., Biercamp, J., Bockelmann, H., Brokopf, R., Brüggemann, N., Casaroli, L., Chegini, F., Datseris, G., Esch, M., George, G.,
784 Giorgetta, M., Gutjahr, O., Haak, H., Hanke, M., Ilyina, T., Jahns, T., Jungclaus, J., Kern, M., Klocke, D., Kluft, L., Kölling, T.,
785 Kornblueh, L., Kosukhin, S., Kroll, C., Lee, J., Mauritsen, T., Mehlmann, C., Mieslinger, T., Naumann, A. K., Paccini, L.,
786 Peinado, A., Praturi, D. S., Putrasahan, D., Rast, S., Riddick, T., Roeber, N., Schmidt, H., Schulzweida, U., Schütte, F., Segura,
787 H., Shevchenko, R., Singh, V., Specht, M., Stephan, C. C., von Storch, J.-S., Vogel, R., Wengel, C., Winkler, M., Ziemen, F.,
788 Marotzke, J., and Stevens, B.: ICON-Sapphire: simulating the components of the Earth system and their interactions at kilometer
789 and subkilometer scales, Geosci. Model Dev., 16, 779–811, https://doi.org/10.5194/gmd-16-779-2023, 2023.
790
791 Howard, L.: Essay on the modifications of clouds, John Churchill & Sons, London, 64 pp., 1803.
792
793 Kaps, A., Lauer, A., Camps-Valls, G., Gentine, P., Gómez-Chova, L., and Eyring, V.: Machine-Learned Cloud Classes From
794 Satellite Data for Process-Oriented Climate Model Evaluation, IEEE Transactions on Geoscience and Remote Sensing, 61, 1-15,
795 4100515, https://doi.org/10.1109/TGRS.2023.3237008, 2023.
796
797 Kuma, P., Bender, F. A.-M., Schuddeboom, A., McDonald, A. J., and Seland, Ø.: Machine learning of cloud types in satellite
798 observations and climate models, Atmos. Chem. Phys., 23, 523–549, https://doi.org/10.5194/acp-23-523-2023, 2023.
799
800 Kurihana, T., Moyer, E., Willett, R., Gilton, D.y, and Foster, I.: Data-Driven Cloud Clustering via a Rotationally Invariant
801 Autoencoder, IEEE Transactions on Geoscience and Remote Sensing, 60, 1-25, 4103325,
802 https://doi.org/10.1109/TGRS.2021.3098008, 2022.
803
804 LeCun, Y., Jackel, L. D., Boser, B., Denker, J. S., Graf, H. P., Guyon, I., Henderson, D., Howard, R. E., and Hubbard, W.:
805 Handwritten digit recognition: Applications of neural network chips and automatic learning, IEEE Communications Magazine,
806 Volume 27, Issue 11, 41-46, https://doi.org/10.1109/35.41400, 1989.
807
808 LeCun, Y., and Bengio, Y.: Convolutional networks for images, speech, and time series, The handbook of brain theory and neural
809 networks, 3361, 10, 1995.
810
811 Lemaitre, G., Nogueira, F., and Aridas, C., K.: Imbalanced-learn: A Python Toolbox to Tackle the Curse of Imbalanced Datasets
812 in Machine Learning, Journal of Machine Learning Research, 18, 1-5, http://jmlr.org/papers/v18/16-365.html, 2017.
813
814 Luo, H., Quaas, J., and Han, J.: Diurnally asymmetric cloud cover trends amplify greenhouse warming, Science Advances, 10,
815 25, https://doi.org/10.1126/sciadv.ado5179, 2024.
816
817 Lenhardt, J., Quaas, J., and Sejdinovic, D.: Marine cloud base height retrieval from MODIS cloud properties using machine
818 learning, EGUsphere [preprint], https://doi.org/10.5194/egusphere-2024-327, 2024a.
819
820 Lenhardt, J., Quaas, J., Sejdinovic, D., and Klocke, D.: CloudViT - Method code and data for the article "CloudViT: classifying
821 cloud types in global satellite data and in kilometre-resolution simulations using vision transformers.", Zenodo,
822 https://doi.org/10.5281/zenodo.12731288, 2024b.
823
824 Met Office: LAND SYNOP reports from land stations collected by the Met Office MetDB System, NCAS British Atmospheric
825 Data Centre, https://catalogue.ceda.ac.uk/uuid/9f80d42106ba708f92ada730ba321831, 2008.
826

827 Met Office: MIDAS: Global Marine Meteorological Observations Data, NCAS British Atmospheric Data Centre,
828 https://catalogue.ceda.ac.uk/uuid/77910bcec71c820d4c92f40d3ed3f249, 2006.
829
830 Paszke, A., Gross, S., Massa, F., Lerer, A., Bradbury, J., Chanan, G., Killeen, T., Lin, Z., Gimelshein, N., Antiga, L., Desmaison,
831 A., Kopf, A., Yang, E., DeVito, Z., Raison, M., Tejani, A., Chilamkurthy, S., Steiner, B., Fang, L., Bai, J. and Chintala, S.:
832 PyTorch: An Imperative Style, High-Performance Deep Learning Library, in Advances in Neural Information Processing
833 Systems 32 (NeurIPS), 8024–8035,
834 http://papers.neurips.cc/paper/9015-pytorch-an-imperative-style-high-performance-deep-learning-library.pdf, 2019.
835
836 Pedregosa, F., Varoquaux, G., Gramfort, A., Michel, V., Thirion, B., Grisel, O., Blondel, M., Prettenhofer, P., Weiss, R., Dubourg,
837 V., Vanderplas, J., Passos, A., Cournapeau, D., Brucher, M., Perrot, M., and Duchesnay, E.: Scikit-learn: Machine Learning in
838 Python, Journal of Machine Learning Research, 12, 2825-2830, https://www.jmlr.org/papers/v12/pedregosa11a.html, 2011.
839
840 Pincus, R., Hubanks, P. A., Platnick, S., Meyer, K., Holz, R. E., Botambekov, D., and Wall, C. J.: Updated observations of clouds
841 by MODIS for global model assessment, Earth Syst. Sci. Data, 15, 2483–2497, https://doi.org/10.5194/essd-15-2483-2023, 2023.
842
843 Platnick, S., Ackerman, S. A., King, M. D., Meyer, K., Menzel, W. P., Holz, R. E., Baum, B. A., and Yang, P.: MODIS
844 atmosphere L2 cloud product (06_L2), NASA MODIS Adaptive Processing System, Goddard Space Flight Center,
845 http://doi.org/10.5067/MODIS/MYD06_L2.061, 2017.
846
847 Platnick, S., King, M.D., Ackerman, S.A., Menzel, W.P., Baum, B.A., Riedi, J.C., and Frey, R.A.: The MODIS cloud products:
848 algorithms and examples from Terra, in: IEEE Transactions on Geoscience and Remote Sensing, Volume 41, Number 2, 459-473,
849 http://doi.org/10.1109/TGRS.2002.808301, 2003.
850
851 Rasp, S., Schulz, H., Bony, S., and Stevens, B.: Combining Crowdsourcing and Deep Learning to Explore the Mesoscale
852 Organization of Shallow Convection, Bulletin of the American Meteorological Society, 101, E1980-E1995,
853 https://doi.org/10.1175/BAMS-D-19-0324.1, 2020.
854
855 Ronneberger, O., Fischer, P., and Brox, T.: U-Net: Convolutional Networks for Biomedical Image Segmentation, in: Navab, N.,
856 Hornegger, J., Wells, W., Frangi, A. (eds) Medical Image Computing and Computer-Assisted Intervention (MICCAI 2015),
857 Lecture Notes in Computer Science, Volume 9351, Springer, Cham., https://doi.org/10.1007/978-3-319-24574-4_28, 2015.
858
859 Rossow, W.B., and Schiffer, R.A.: ISCCP cloud data products, Bull. Amer. Meteorol. Soc., 71, 2-20, 1991.
860
861 Sassen, K., Wang, Z., and Liu, D.: Global distribution of cirrus clouds from CloudSat/Cloud-Aerosol Lidar and Infrared
862 Pathfinder Satellite Observations (CALIPSO) measurements, J. Geophys. Res., Volume 113, D00A12,
863 https://doi.org/10.1029/2008JD009972, 2008.
864
865 Stevens, B., Giorgetta, M., Esch, M., Mauritsen, T., Crueger, T., Rast, S., Salzmann, M., Schmidt, H., Bader, J., Block, K.,
866 Brokopf, R., Fast, I., Kinne, S., Kornblueh, L., Lohmann, U., Pincus, R., Reichler, T., and Roeckner, E.: Atmospheric component
867 of the MPI-M Earth System Model: ECHAM6, Journal of Advances in Modeling Earth Systems, 5, 2, 146-172,
868 https://doi.org/10.1002/jame.20015, 2013.
869
870 Touvron, H., Vedaldi, A., Douze, M., and Jegou, H.: Fixing the train-test resolution discrepancy, 33rd Conference on Neural
871 Information Processing Systems (NeurIPS 2019), Vancouver, Canada, https://doi.org/10.48550/arXiv.1906.06423, 2019.
872
873 Tzallas, V., Hünerbein, A., Stengel, M., Meirink, J. F., Benas, N., Trentmann, J., Macke, A.: CRAAS: A European Cloud Regime
874 dAtAset Based on the CLAAS-2.1 Climate Data Record, Remote Sensing, 14, 5548, https://doi.org/10.3390/rs14215548, 2022.
875
876 Unglaub, C., Block, K., Mülmenstädt, J., Sourdeval, O., and Quaas, J.: A new classification of satellite-derived liquid water
877 cloud regimes at cloud scale, Atmos. Chem. Phys., 20, 2407–2418, https://doi.org/10.5194/acp-20-2407-2020, 2020.
878

Vaswani, A., Shazeer, N., Parmar, N., Uszkoreit, J., Jones, L., Gomez, A.N., Kaiser, L., and Polosukhin, I.: Attention Is All You Need, arXiv preprint, https://doi.org/10.48550/ARXIV.1706.03762, 2017.

WMO: International cloud atlas, Manual on the Observation of Clouds and Other Meteors (WMO-No. 407), available at: https://cloudatlas.wmo.int (last access: 27 February 2020), 2017.

WMO: Manual on Codes, Volume I.1 – International Codes, Annex II to the WMO Technical Regulations, Part A – Alphanumeric Codes (WMO-No. 306), ISBN: 978-92-63-10306-2, available at: https://library.wmo.int/idurl/4/35713, 2019.

Wood, R.: Stratocumulus clouds, Monthly Weather Review, 140, 8, 2373–2423, https://doi.org/10.1175/MWR-D-11-00121.1, 2012.

Zantedeschi, V., Falasca, F., Douglas, A., Strange, R., Kusner, M. J., and Watson-Parris, D.: Cumulo: A Dataset for Learning Cloud Classes, Tackling Climate Change with Machine Learning Workshop, 33rd Conference on Neural Information Processing Systems (NeurIPS 2019), Vancouver, Canada, https://doi.org/10.48550/arXiv.1911.04227, 2019.

Zhang, J. L., Liu, P., Zhang, F., & Song, Q. Q.: CloudNet: Ground-based cloud classification with deep convolutional neural network, Geophysical Research Letters, 45, 8665–8672, https://doi.org/10.1029/2018GL077787, 2018.

Zhao, H., Gallo, O., Frosio, I., and Kautz, J.: Loss functions for image restoration with neural networks, IEEE Transactions on computational imaging, 3, 1, 47–57, https://doi.org/10.1109/TCI.2016.2644865, 2016.